ADVANCING
EARTH AND
SPACE SCIENCE

JGR Solid Earth

RESEARCH ARTICLE

Key Points:

- GPS stations constrain trends, seasonal and nonseasonal variability in vertical land motion (VLM) across the Earth's land surface
- GPS Imaging provides robust VLM estimates and more completely assesses spatial and temporal signal uncertainty and variability
- Average VLM is positive on the land areas and subsidence elsewhere, but average non-GIA VLM is subsidence on average and uplift elsewhere

GPS Imaging of Global Vertical Land Motion for Studies of Sea Level Rise

William C. Hammond[1] , **Geoffrey Blewitt[1]** , **Corné Kreemer[1]** , and **R. Steven Nerem[2]**

[1]Nevada Geodetic Laboratory, Nevada Bureau of Mines and Geology, University of Nevada Reno, Reno, NV, USA, [2]Ann and H.J. Smead Department of Aerospace Engineering Sciences, Colorado Center for Astrodynamics Research, University of Colorado, Boulder, CO, USA

Abstract We estimate the rates and patterns of vertical land motion (VLM) on all locations on Earth's land surface using GPS Imaging. The solution is based on a large database of uniformly processed GPS data from solutions that are aligned to the International Terrestrial Reference Frame. We provide global maps and estimates of VLM at all tide gauges of the Permanent Service for Mean Sea Level to better constrain the difference between geocentric and relative sea level rise. To enable critical assessment of the VLM estimate, the temporal and spatial contributions to rate uncertainty and variability are generated and included for every gauge. Seasonality and trends of uplift are assessed and found to be strongly correlated with observations from gravity data suggesting that loading from the terrestrial hydrosphere is a dominant driver of non-glacial isostatic adjustment (non-GIA) VLM. Although stations are dominantly concentrated at subsiding parts of continents, GPS Imaging geographically balances VLM signals, correcting for bias associated with network distribution. This allows us to make a global assessment of the budget of uplift and subsidence attributable to GIA and non-GIA sources. We show that the surface motion of the continents is on average upward, implying that the unobserved areas (composed of the ocean basins and ice-covered areas) move on average downward with respect to Earth center. However, after correcting for the GIA the reverse is true, and observed areas subside on average implying that the unobserved areas undergo net non-GIA-related uplift.

Plain Language Summary Sea level rise is a global problem. To project its impacts on coastal communities and understand its physical sources requires observation of active vertical land motion across all of the Earth's continents. Vertical motion of the land directly affects coastal relative sea level rise and has many possible driving mechanisms, for example, plate tectonic movements, earthquakes, subsidence from aquifer withdrawal, postglacial rebound, or other active geophysical processes. The precision, coverage, and prevalence of open data holdings that are now available from GPS stations around the world provide a unique data set for constraining these movements on a global scale. Since GPS stations around the world are very heterogeneously distributed on land our analysis emphasizes robust methods to obtain geographically balanced estimates of a global field. We use these estimates to show the rates and patterns of vertical land movement and evaluate the balance of uplift and subsidence across the Earth's surface. We provide maps and rates at over 2,300 tide gauges around the world which will be used to project the rates of sea level rise into the future.

1. Introduction

The impact of sea level rise on coastal communities depends critically on rate of sea surface elevation change in relation to the coastal land. Thus, vertical land motion (VLM) can either exacerbate or reduce sea level changes, affecting its impact in different ways, in different parts of the world (e.g., Conrad, 2013; Douglas, 2001; Wöppelmann & Marcos, 2016). In addition, geographically variable VLM complicates reconstruction of Global Mean Sea Level changes from tide gauge data (e.g., Hamlington et al., 2016) and connection of satellite radar altimetry measurements of the ocean surface to coastal relative sea level (RSL) rise (Mitchum, 2000; Nerem et al., 2010). Thus, understanding the rate, pattern, and variability of VLM near coasts leads to a direct improvement of RSL estimates (Cazenave et al., 1999; Ray et al., 2010; Santamaría-Gómez et al., 2017) and process-based projections of it into the future (Church et al., 2013).

Many processes contribute to vertical motion of Earth's surface (Pfeffer et al., 2017). The one with the greatest impact on global sea level is the steady motion arising from glacial isostatic adjustment (GIA) following the loss of the continental ice sheets, which has horizontal wavelengths of thousands of kilometers (e.g., Caron et al., 2018; Milne & Mitrovica, 1998; Peltier et al., 2015). However, many other processes contribute to VLM and these have a variety of rates, patterns, and wavelengths. These include tectonic uplift (e.g., Beavan et al., 2010; Bürgmann et al., 2006; Marshall et al., 2017; Serpelloni et al., 2013), isostatic adjustment following erosion (England & Molnar, 1990; Small & Anderson, 1995), sediment loading (Ivins et al., 2007), and changes in mantle flow or dynamic topography (Arnould et al., 2018; Faccenna & Becker, 2010; Hoggard et al., 2016; Kreemer et al., 2020). Shorter term and unsteady VLM changes can arise from elastic response to contemporary ice loss owing to climate change (e.g., Argus et al., 2011; Jiang et al., 2010; Larsen et al., 2005), trends in storage within aquifers and hydrocarbon reservoirs (Faunt, 2009; White & Morton, 1997), surface loading owing to changes in the terrestrial hydrosphere (Amos et al., 2014; Borsa et al., 2014; van Dam et al., 2001), sediment compaction (Carbognin et al., 2005; Dixon et al., 2006; Johnson et al., 2020), and earthquake cycle deformation (e.g., Burgette et al., 2009; Mazzotti et al., 2007; Smith-Konter et al., 2014), to name a few. Some of these processes, such as aquifer depletion, can be caused or exacerbated by human activity (Sneed et al., 2013). Thus, while GIA represents the single largest factor driving contemporary VLM, many other processes contribute, making direct measurement to capture its full complexity and time variability necessary. Here, we evaluate the budget of VLM on a global scale to assess how much of it is attributable to non-GIA processes.

Increasingly, global data sets and models are being brought together to improve understanding and project regional sea level rise into the future (Hamlington et al., 2020). To best support and accelerate these efforts, VLM products that are available with global scope are needed, with the greatest possible coverage and precision. Recent improvements have resulted from the continued proliferation of high-precision GPS networks, which are trending toward global coverage with stations having longer records (up to 25 years) at a greater number of locations. Network improvements are coupled with developments in analysis, software, data products, and shifts toward open data policies which continue to improve the estimates of trends in the data for multidisciplinary science applications (Blewitt et al., 2018). These improvements allow imaging of VLM with GPS at resolutions that have utility for regional assessment of sea level rise in a large fraction of Earth's coastlines. However, owing to the heterogeneous distribution of stations and complexity of the signals questions remain about how precise are the VLM estimates at any given location.

Here, we present an analysis of a globally extensive database of GPS data, from which we derived vertical rates using the MIDAS trend estimator (Blewitt et al., 2016). From these rates, we estimate a VLM field using GPS Imaging and a weighted median interpolation method (Hammond et al., 2016). These methods capture VLM signals by relying on robust nonparametric (nonleast squares) methods which are insensitive to seasonality, undocumented steps in the time series, outlier positions, or velocities. The estimates provide VLM at any location, the precision of which depends on several factors, including distance to nearest GPS station, number of nearby stations, duration of observation at those stations, and spatial and temporal variability of land motion. We pay special attention to quantifying the uncertainties in VLM and provide metrics that allow users to identify sources of uncertainty. These results can be used to correct trends seen at tide gauges, identify gauges not effected by VLM, or in analyses where trends from tide gauges, and satellite altimetry are compared to VLM (Cazenave et al., 1999; Nerem & Mitchum, 2002; Ray et al., 2010). They can also be combined with constraints from other techniques (e.g., InSAR and leveling) that work at shorter geographic scales to align constraints to the global reference frame (e.g., Bekaert et al., 2018; Hammond et al., 2018; Shirzaei & Bürgmann, 2018).

2. Data

2.1. GPS Data Set, Data Processing, and Rate Estimation

We base this analysis on a set of positions derived from continuously operating GPS stations processed by the Nevada Geodetic Laboratory (Blewitt et al., 2018). The holdings include RINEX data files from hundreds of GPS networks around the world with >19,000 stations and ~45,000,000 daily RINEX files. The data set was processed to obtain 24-h position solutions using point positioning (Zumberge et al., 1997) implemented in the GipsyX 1.0 software (Bertiger et al., 2020). Auxiliary files included Repro3 final orbits, clocks,
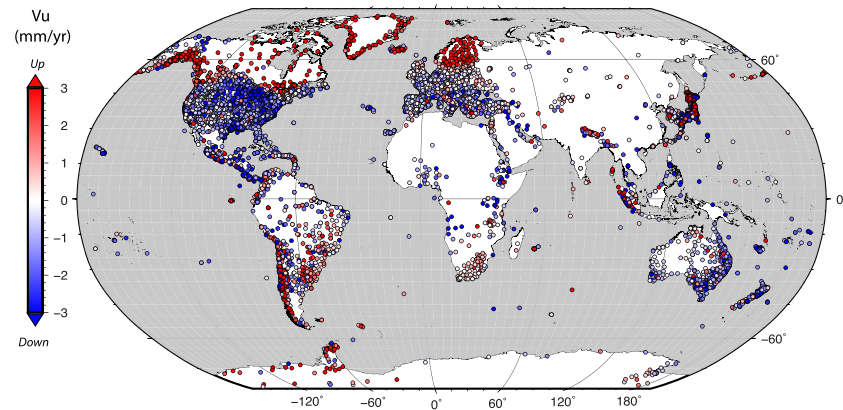
Figure 1. Distribution of the GPS stations for which data are processed by the Nevada Geodetic Laboratory. The color indicates the MIDAS vertical rate available for this analysis.

and other products from the Jet Propulsion Laboratory. All the products are based on, and the solutions are aligned to, the IGS14 realization (Rebischung et al., 2016) of the ITRF14 reference frame (Altamimi et al., 2016). To correct for tropospheric effects, we used the VMF1/ECMWF mapping function with elevation-dependent data weight, nominal dry and wet zenith delays from the numerical weather model (Boehm et al., 2006). Antenna adjustments were made with the IGS14 ANTEX calibration table that has a new algorithm that corrects for antenna and radome fields available in RINEX headers (Schmid et al., 2007). The models include adjustments for solid Earth tides, ocean and atmospheric tidal loading, but not nontidal ocean or atmospheric loading. Additional details about treatment of metadata, data editing, ambiguity resolution, antenna phase center calibrations, and estimation strategy including the atmospheric parameters are provided in Kreemer et al. (2020) and are not repeated here.

To estimate the rate of vertical movement, we use the nonparametric MIDAS algorithm (Blewitt et al., 2016) on the IGS14-aligned time series. MIDAS calculates the median trend from the difference in pairs of vertical position data with intersample duration of ~1 year. This makes the MIDAS rates insensitive to seasonality and steps in the time series even if they are undocumented, as long as the steps are sparse enough in time. The method is robust in the sense that the final result is insensitive to outliers up to a breakdown point (up to ~25% incorrect data). The resulting velocity field is characterized by fewer stations with outlier velocities, making them more suitable for imaging, geophysical modeling, and interpretation (e.g., Hammond et al., 2016). We base the analysis presented here on the MIDAS file downloaded from our own GPS data products system on December 22, 2020. This file has 17,172 stations with sufficient data to obtain a MIDAS velocity (Figure 1) and forms the basis for estimation of a VLM field.

The updated models and products used in our analysis have, compared to the previous generation of solutions in IGS08, resulted in significant reductions in RMS residual scatter of vertical position time series. The improvement is in part due to more effective partitioning of signals between atmospheric effects and real Earth motion (Martens et al., 2020), which translate directly to velocity precision and reduction in bias associated with sources not related to solid Earth motion. All the derived solutions produced by NGL are available at http://geodesy.unr.edu, including time series, time series plots, station maps, tables of site coordinates and durations of observation, and MIDAS velocities.

2.2. Site Selection and Coverage

We omit from the data set stations that have time series duration shorter than 3.5 years and mean completeness (number of observations days per year divide by 365 days) of less than 30%. We omit these stations because they offer less constraint on VLM and keeping them in our database of station locations may give an overly favorable picture of the spatial distribution of stations which we analyze below. After these exclusions, 90% of the stations have completeness greater than 68%. The median/maximum time series duration is 10.2/26.5 years, 90% have their first position on or after the year 2002.0, and the median midtime of the
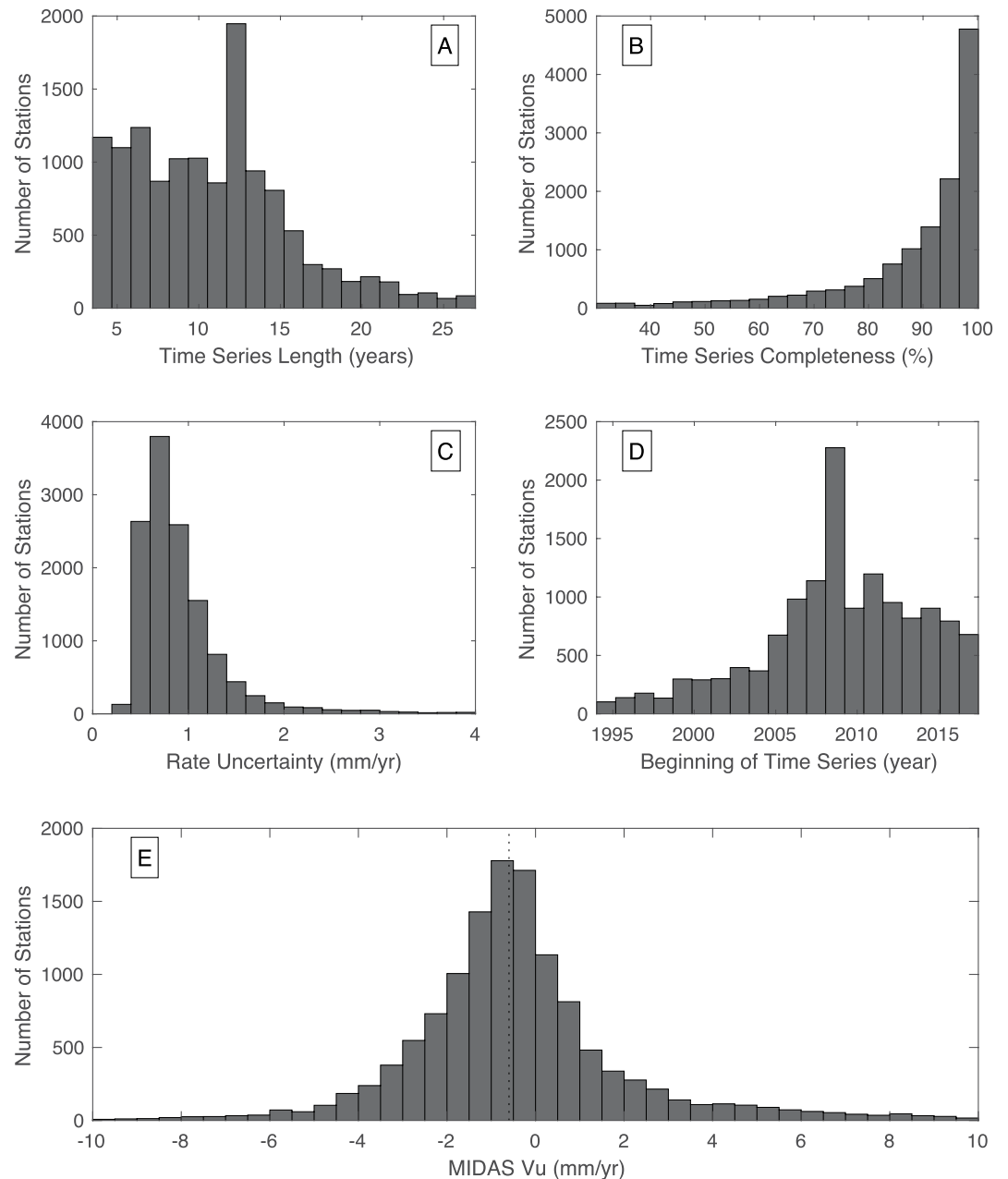
Figure 2. Histograms of statistics for vertical GPS time series used in this analysis. (a) Time series duration in years. (b) Percent time series completeness, that is, number of days of data divided by number of days between first and last day of time series. (c) Uncertainty in MIDAS vertical rate. (d) Decimal year of earliest data in time series. (e) MIDAS velocity. Dotted vertical line in (e) indicates median vertical velocity of -0.60 mm year^{-1}.

time series is 2014.7 (Figure 2). Thus, the data constrain VLM that occurred mostly after 2002.0. We also omit stations whose motion is known to us to not be representative of the solid Earth. For example, stations on flowing ice that have been deployed to study or serve as reference on glaciers in Antarctica or Greenland, and stations on oil platforms, but these collectively affect only 29 stations.

GPS Imaging relies on Delaunay triangulation of the network, which performs best when stations are not collocated. Therefore, prior to imaging we decluster the stations, creating single representative met-astations with a vertical rate that is the weighted median value in the cluster when stations are within 0.1 km of one another. The uncertainty of the cluster rate is determined as if it were a weighed mean of

the contributing rates, where the weights are one over the uncertainties, making large uncertainty rates unlikely to contribute. The median difference between the maximum and minimum rate in a cluster (excluding cases with only one station in the cluster) is 0.7 mm year^{-1} and 90% are less than 2.9 mm year^{-1}. Though a few maximum differences are large they are usually filtered in this declustering stage or later if they are rate outliers. Most clusters have only two stations so the one with the lower uncertainty will be selected via the weighted median. This and the selection criteria described above results in a reduction in the effective number of stations to 13,006, where 3.2% of stations represent clusters. In this set, 98% of the vertical rate uncertainties are less than 2 mm year^{-1}, and 68% are less than 1 mm year^{-1} (Figure 2).

Most of the VLM signal lies within a narrow range, with 97% between −10 and 10 mm year^{-1}. A histogram of the velocities is shown in Figure 2. The median vertical rate at GPS stations is −0.60 mm year^{-1}. The slightly negative median is significant with respect to the uncertainty in the estimate of the sample median. However, it is negative owing to the bias introduced by station concentrations in subsiding areas such as the central United States which is widely affected by GIA fore-bulge collapse over a large segment of the country. Europe subsides in the southern half of the continent for similar reasons (Lambeck et al., 1998; Peltier et al., 2015). GPS Imaging estimates VLM on a grid which mitigates the bias associated with station concentrations. This is important because, as we show below, the median VLM of the continent is strongly positive and would be misrepresented if the heterogeneous station distribution were not taken into account.

2.3. How Much of the Land Area and Coasts Are Covered?

Owing to the heterogeneous station distribution, the quality of VLM constraint varies greatly among and within the continents. Figure 1 shows that the density of station coverage is much greater in the Northern Hemisphere, especially in North America and Europe. The continental interiors have large areas that are poorly sampled, especially in Asia and Africa. To objectively portray the variability in geographic coverage, we show in Figure 3 the distance from every point on land to the nearest GPS station that passed our exclusion criteria. These distances range from about zero to a maximum of 13.9° (∼1,540 km) in the Saharan Desert of northern Africa near the border between Chad and Libya.

The percentage of land area that is within a given distance to a GPS station in shown in Figure 3b. This chart is created by summing the area of Figure 3a that has values less than or equal to the value on the horizontal axis of Figure 3b, excluding oceanic areas. For example, on the major land masses, 52.7% of land area has no GPS station within a distance of 2° (∼222 km), and 84.5% of land area has a GPS station within 5° (blue bars in Figure 3b). However, the perimeter of continents tends to be better covered, because of the concentration of populations (and GPS stations) near coasts. So, we repeat the analysis except by taking steps of median size 28 km along the coastlines, summing the length of linear coasts that are within the given distances on the horizontal axis of Figure 3b, divided by the total length of all perimeters (red bars in Figure 3b). This indicates that across the globe 73.9% percent of the linear coastlines have a GPS station with 2°, and 93.0% have a GPS station within 5°.

Despite the presence of hundreds of GPS stations on islands, the oceans are generally poorly covered. In the ocean basins, the maximum nearest distance from a permanent GPS station is 26.7° (∼2,970 km), about twice the maximum distance on land. That location is in the southeast Pacific Ocean (at −49.75° latitude, −137.75° longitude). For this reason, we omit the ocean basins from the imaging. While sea-floor geodesy is becoming a more viable mode for observing Earth deformation (e.g., Bürgmann & Chadwell, 2014), the GPS networks are unlikely to proliferate onto the sea floor at the rate they have on land. Thus, we expect the ocean/land sampling bias to be a long-lived feature in the analysis of global VLM. For similar reasons, we block out areas covered with ice, including the interiors of Greenland and Antarctica, since there are no bedrock observations there. However, in Antarctica, we preserve the area of the Transantarctic and Ellsworth mountains which have some bedrock GPS sites that can be used to measure uplift (Argus et al., 2011; Bevis et al., 2009).
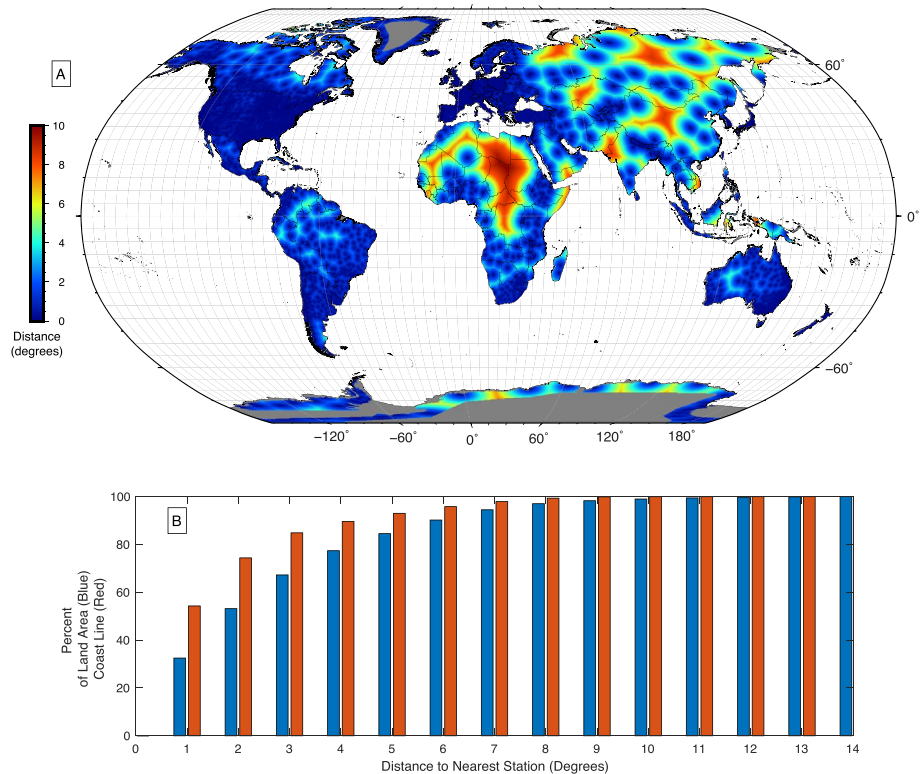
Figure 3. (a) Color indicates distance to nearest GPS station. White areas are ocean basins and gray areas are masked out areas covered by ice sheets. (b) Cumulative percent area having distance less than or equal to value on the horizontal axis (blue), and cumulative percent of linear coasts having distance less than or equal to value on the horizontal axis (red). See text for discussion.

3. Analysis

3.1. GPS Imaging

A benefit of GPS Imaging is that stations in the continental interiors are used to obtain insights about variability of signals and processes that effect VLM at the coast. The method has been documented elsewhere (Hammond et al., 2016), but we briefly describe the essential aspects here since they may impact the interpretation of the images. There are two major steps. In the first step, we apply weighted median spatial filtering to the vertical MIDAS GPS rates, and in the second step, we perform the imaging, where the same algorithm is applied to points on a grid.

In both steps, we require a spatial structure function (*ssf*) which represents the degree of similarity in VLM rates as a function of distance between locations. The *ssf* itself is a function of distance Δ_{ij} between GPS station i and evaluation point j, which varies from 0° to 180°. The form of the *ssf* is based on the expectation that two GPS stations in the same location will have the same rate, and stations separated by great distance are expected to have weak similarity. Stations in the same location will be similar to the degree expected from their aleatory uncertainties. Stations separated by a great distance will have less similarity but are sampled by the global GPS network, so there is still some degree of expectation of similarity (e.g., described by the histogram in Figure 2e). In our construction of the *ssf*, it is forced to have a form such that $ssf(0°) = 1$ and $ssf(180°) = 0$. We determine the values of the *ssf* between $\Delta_{ij} = 0°$ and 180° empirically from the data. It can have any shape, but we require that it decreases monotonically. In the supplementary materials, we describe in detail how we generate the *ssf* for each continent and additionally one for the entire data set to use at locations not on major land masses.

Once the *ssf* is determined, we use it to estimate the weighted median velocity $\hat{v}_j$ at each evaluation location *j*:

$$w_{ij} = \frac{ssf\left(\Delta_{ij}\right)}{\sigma_i} \tag{1}$$

$$w'_{ij} = \frac{w_{ij}}{\sum w_{ij}} \tag{2}$$

$$\hat{v}_j = \text{weighted median}\left(v_i, w'_{ij}\right) \tag{3}$$

where v_i are the set of vertical MIDAS velocities at GPS stations *i* that are connected to the evaluation point *j* via Delaunay triangulation. For each evaluation location, the weights are computed using Equation 2 using the MIDAS rate uncertainty σ_i. To perform the filtering in the first step, we replace each velocity v_i with the weighted median of the original velocities at neighboring locations.

In the second step, we estimate the VLM rate at grid point locations using the filtered data from the neighboring GPS stations as connected via an ad hoc Delaunay triangulation with the grid point location temporarily added to the list of station locations. We calculate the weighted median of the filtered MIDAS station velocities adjacent to the evaluation point. This estimate is free from prior assumption about the functional form of the signal since it is made independently at each grid point. This is desirable when imaging complex fields that may contain signals from multiple processes that operate at different amplitudes and wavelengths, possibly by orders of magnitude (e.g., GIA vs. aquifer deformation). It also makes the estimate insensitive to velocity outliers and geographically local, sensitive to the nearest GPS stations, and resolution dependent more on station density than on grid parameterization.

3.2. Spatial Variability of VLM Signals

In practice, the importance of the *ssf* is low when the GPS network is dense and velocity uncertainties are similar, so the weights will vary little among the stations connected to the evaluation point. However, the importance of the *ssf* is larger where the GPS station spacing is greater than the horizontal length scale of the VLM signal, and/or the station density is variable. We can quantify this spatial part of the VLM rate uncertainty as

$$\hat{\eta}_j = \text{median}\left(ssf\left(\Delta_{ij}\right)\right) \tag{4}$$

which is unitless since it is the median *ssf* value (all between 0 and 1) at the set of distances Δ_{ij} from stations *i* connected to the evaluation point *j*. In Figure 4, we show at every grid point on land the value of $\hat{\eta}_j$. This map illustrates a factor unrelated to the uncertainties in the GPS velocities that influences how well the VLM is resolved at each location. Maps of $\hat{\eta}_j$ can be thought of as a replacement for a checkerboard test of the kind commonly used in geophysical imaging. It is more direct than a checkerboard test because it does not presume any specific length scale or pattern of VLM signal (such as checkers) against which to compare resolution. Rather it compares the network to the dominant wavelength of actual signal observed in the VLM field. We note that the nearest GPS station may have a larger *ssf* value and contribute to the local VLM estimate, so $\hat{\eta}_j$ may be a somewhat pessimistic measure in some locations. When we create an alternative map (not shown) keyed to the minimum *ssf* instead of the median *ssf*, it has higher values in the sparsely covered regions, suggesting better resolution of VLM but based only on the nearest station. We construct Equation 4 to represent something close to the center and body of constraint on VLM at each location, instead of to its single nearest station.

In Figure 4, blue domains represent places where the GPS stations are generally dense enough to resolve horizontal wavelengths of VLM signal observed in the data. These areas include North America (excluding the Arctic Archipelago and Greenland), most of Africa near the coast, southern Europe, Britain, Japan, and
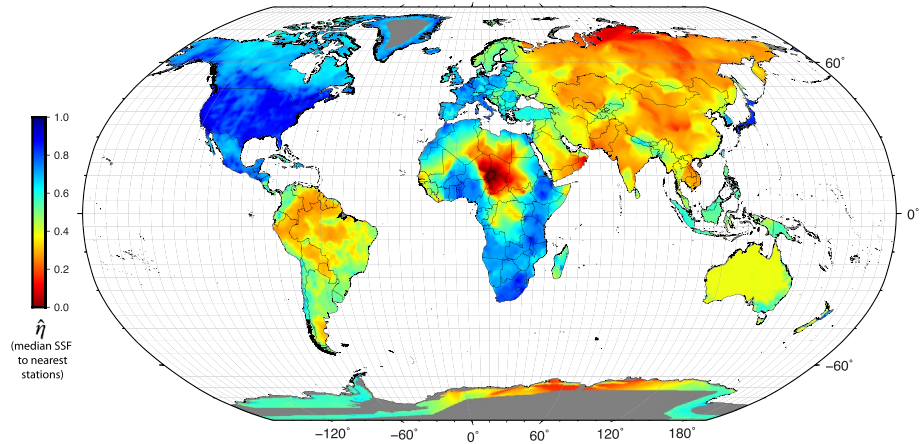
Figure 4. Median value of the spatial structure function (*ssf*) at distances to the set of nearest GPS stations connected to each evaluation grid point (pixel) on the map. Masked areas are same as in Figure 3. Blue (red) areas have generally high (low) GPS station density compared to the dominant horizontal wavelength of vertical land motion signals.

northeast New Zealand. Some areas including most of Asia (aside from South Korea) and parts of Antarctica are not well covered. Some areas with many stations have only medium quality of coverage according to the $\hat{\eta}_j$ parameter, these include South America, Australia, and parts of Antarctica.

3.3. Seasonal VLM Variability

Seasonality in vertical motion of the Earth surface has its source in multiple processes, including loading from the terrestrial hydrosphere, atmosphere, thermal changes, and aquifer pumping (e.g., Blewitt & Lavallée, 2002; Bos et al., 2010; Davis et al., 2012; Prawirodirdjo et al., 2006; van Dam et al., 2001). Here, we estimate the amplitude and phase of annual vertical motion from the residual time series for each station after removal of other signals discussed above such as trends, steps, and exponential transients from large earthquakes. We use the relation:

$$x(t) = S_1 \sin(2\pi t) + C_1 \cos(2\pi t) \tag{5}$$

where $x(t)$ is the vertical position as a function of time t. We solve for sine S_1 and cosine C_1 terms then convert them into annual amplitude A_u and phase ϕ_u of the vertical signal:

$$A_u = \sqrt{S_1^2 + C_1^2} \tag{6}$$

$$\phi_u = \left(atan2(S_1, C_1) + \pi\right)\frac{365}{2\pi} \tag{7}$$

where *atan*2 is the four-quadrant inverse tangent, taken modulo 2π. For convenience in interpretation of the phase in terms of seasons, we multiply by the factor $365/2\pi$ to convert from radians to the day of calendar year ϕ_u. To simplify comparison to gravity data, which exhibit seasonal maximum equivalent water heights when the seasonal GPS station height attributable to loading is at minimum, we add π so that the resulting day represents the time where GPS station elevation is minimum. Because S_1 and C_1 are inferred from multiyear time series, these are the mean annual amplitudes and phases for the station across the period of observation.

We then use GPS Imaging to perform robust filtering and interpolation to map ϕ_u and A_u on the continents (Figure 5). The amplitudes are large (8 mm and greater) in locations where seasonal precipitation is large such as in the Amazon Basin, southern Alaska, southeast Asia, and sub-Saharan West Africa. The
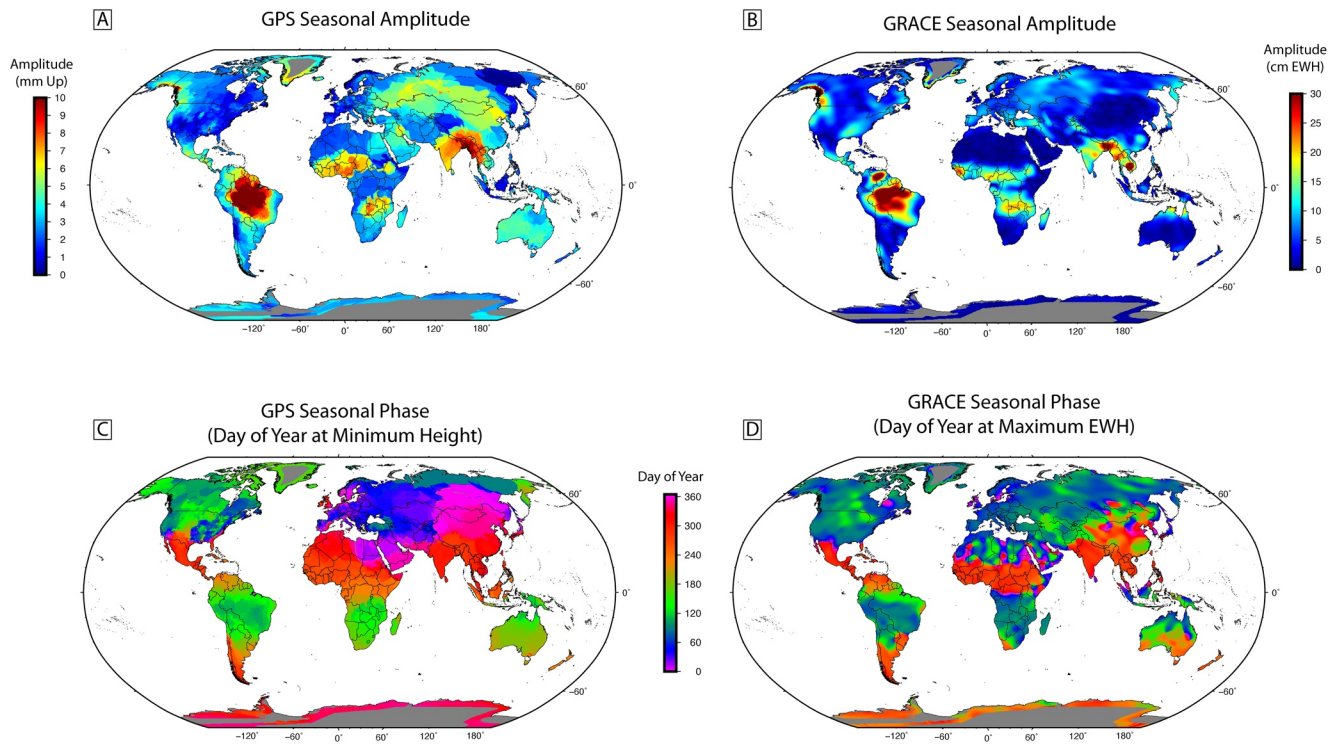
Figure 5. (a) Amplitude and (c) phase of annual oscillation of GPS VLM, depicted as day of year. (b) Amplitude and (d) phase of annual Gravity Recovery and Climate Experiment (GRACE) signal in cm equivalent water height (Loomis et al., 2019). There is a very strong global correspondence between the amplitude and phase of seasonal signals in GPS and GRACE. Note that factor of 10 change in scale between GPS and GRACE and that phase of GPS refers to day of year the station is at its minimum height in its cycle. See text for discussion.

amplitudes are small (2 mm or less) in relatively dry regions such as the Saharan Desert, southwest United States, and southern Europe.

These signals show a strong correspondence to the annual terms resolved from Gravity Recovery and Climate Experiment (GRACE) satellite data (Luthcke et al., 2013; Watkins et al., 2015). We used time series from the mascon solutions (Loomis et al., 2019) to solve for the annual amplitude and phase using the same method as for the GPS time series. We interpolate the result from mascon centers to a regular grid to map the seasonal amplitude and phase (the day of year the equivalent water height is at a maximum—Figure 5). For the amplitudes, we see that there is a very strong spatial correlation between GPS and GRACE seasonal amplitudes, suggesting the dominance of seasonal mass loading changes driving the GPS seasonal vertical motion.

For the phase signals, there is a strong dependence on latitude, and for large sectors of the Earth's terrestrial surface, the timing is strongly associated with timing of seasonal precipitation. There is a very strong correlation between the timing of GPS and GRACE changes, again consistent with seasonal hydrological loading being the driving mechanism. Areas with a large proportion of their precipitation occurring in Northern Hemisphere winter such as northern North America and Europe have their lowest positions in late spring when the most water has accumulated and driest periods in the late autumn. Areas with a large proportion of their precipitation budgets coming from summer monsoon precipitation such as southeast Asia, the southwest United States, Mexico, and northern Africa have their driest periods in the spring, out of phase with other areas. There is a lack of symmetry between the hemispheres. For example, Amazonian South America (between −30° and 0°) and northern North America (between 40° and 70°) are both at minimum elevation near day of year 150. This is the time of Northern Hemisphere spring and Southern Hemisphere autumn, but in both locations is the time of year that ends the season with heaviest precipitation.

The seasonal linking of VLM and hydrological loading indicates that they are also linked during multiannual changes in hydrological loading, such as drought periods. Thus, trend changes in terrestrial hydrology

can impart trend changes in VLM, and the duration of those changes depends on the duration of change in precipitation. These inflections can be observed with GPS as nonlinear signals (Adusumilli et al., 2019; Borsa et al., 2014; Hammond et al., 2016; Silverii et al., 2016) which we examine on a global scale in the next section.

3.4. Nonseasonal VLM Variability

Owing to various factors including hydrologic loading, there is often uncertainty about the extent to which trends in GPS data reflect long-term steady geologic movement. An indication that GPS data may not represent long-term geodynamic processes is when its velocity is not constant, suggesting that long-term motion is overprinted by transient processes. We can quantify the steadiness of GPS velocities by computing for each time series an index of rate variability. For each time series, we take 2-year long subintervals and compute the MIDAS rate for each interval. We start with the first 2 years of the time series, then select a new interval by shifting the window forward in time by 1 month and repeat the process until the window reaches the end of the time series. The 2-year window size is selected because it is long enough to include enough data pairs to compute the MIDAS rate, yet short enough so that many rate samples can be generated for the time series in our data set. The result is a time series of velocity for the station which indicates how the rate varied over the observation period. Because of the properties of the MIDAS trend estimator, this variability index is insensitive to outliers and annual periodicity. Hence, this index is a robust measure of *nonseasonal velocity variability* (v_i) in velocity.

The index is computed as the median absolute deviation (MAD) of the values in the velocity time series:

$$v_i = \text{MAD}\left(v\left[t_k - 1.0, t_k + 1.0\right]\right) \tag{8}$$

which has units of mm year^{-1}. Here, v is the MIDAS velocity obtained from the 2-year interval of the time $[t_k - 1.0, t_k + 1.0]$ centered on t_k, which are decimal years. The index k specifies which 2-year interval of the time series is selected. Using the MAD as opposed to the standard deviation adds an additional layer of robustness since it is less sensitive to outlier rates. Stations with complicated vertical motion history will have larger v_i, while stations with very linear trends have low v_i. Examples for two stations are shown in Figure 6. For station QUIN, the variability is relatively high, its vertical time series exhibits several changes in course and does not convincingly describe a steady trend ($v_i = 4.0$ mm year^{-1}). The station TONO in central Nevada has a period of very linear vertical motion with a brief excursion in 2003–2005 but has low overall variability ($v_i = 1.1$ mm year^{-1}). Figure 7 shows a histogram of v_i for all stations, indicating 50% are less than 1.4 mm year^{-1}. A histogram of v_i normalized by the uncertainty in the MIDAS rate for the entire time series and multiplied by 1.4826 to scale the MAD so it represents a standard deviation in a Gaussian distribution indicates that 43.2% have values greater than 2. This indicates that the temporal variability of vertical rate is significant for a large fraction of the stations. However, only ∼5% have variability higher than station QUIN. To see where on Earth variability most affects the rates we perform the imaging on v_i to obtain gridded values $\hat{v}_j$ (Figure 7). The robust imaging prevents individual stations with outlying v_i dominating, so only variability present in multiple adjacent stations and representative of large-scale land motion are seen.

We see high variability in locations that are known to be influenced by hydrological mass changes (Figure 7). For example, previous work based on GRACE and GPS saw that hydrological loading changes drive seasonal and multiannual motions in the Amazon basin of South America (Ferreira et al., 2020; Fu et al., 2013). Since $\hat{v}_j$ represents nonseasonal changes in motion the Amazon variability indicates multiyear loading changes that affect rates on a near-continental scale. There is also high variability in other areas affected by hydrological mass changes, including the Greenland coast, Antarctica, and Central California. In some cases, variability can be high in regions where VLM is low, and vice versa. For example, we see low variability in central Canada, where uplift is caused by GIA, which is steady over time.

3.5. Spatial Scatter in VLM Rate

An independent indicator of uncertainty in VLM estimates is the spatial variability of vertical rates within clusters that are used to image rates at evaluation points. Because our estimates are based on medians of
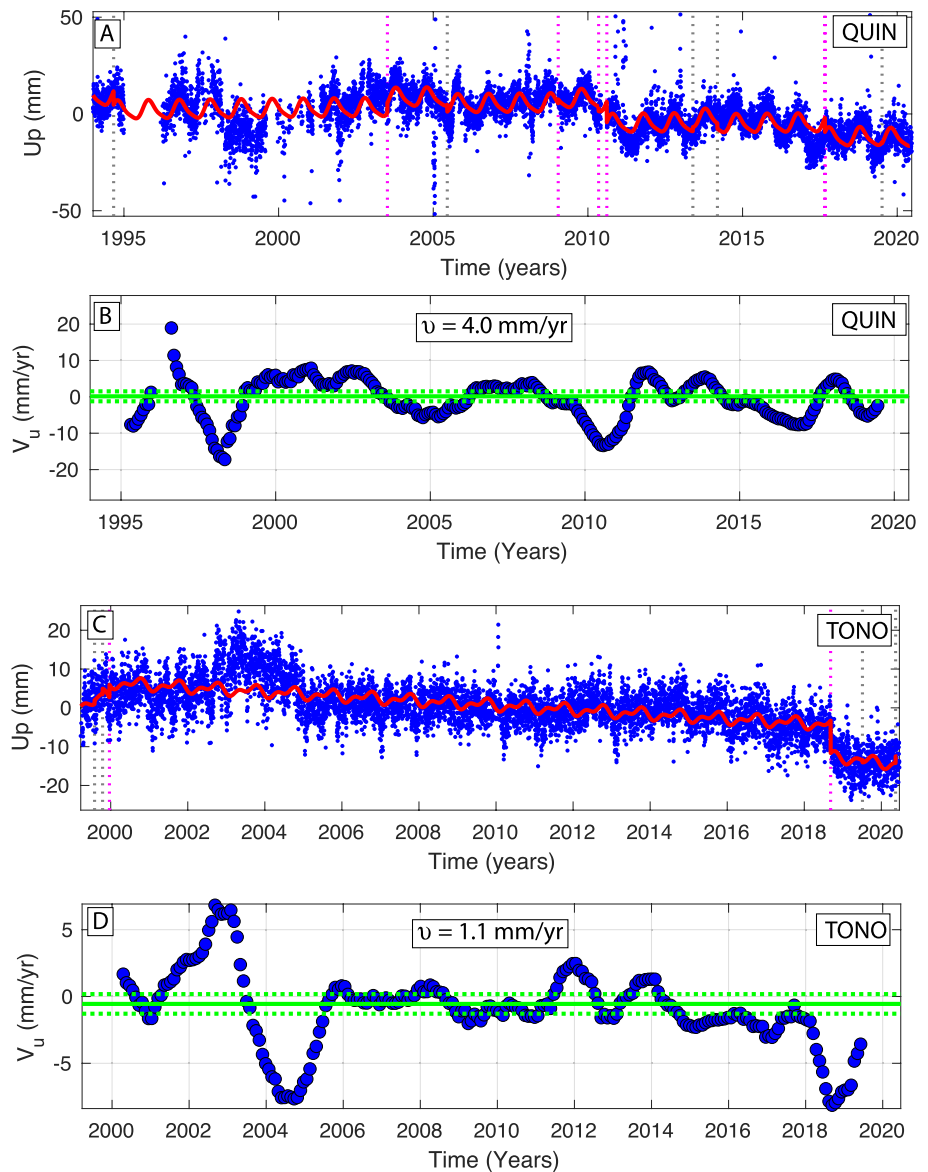
Figure 6. Two examples of GPS vertical position (a and c) and velocity (b and d) time series, for station QUIN (a and b) and TONO (c and d), which have very different degrees of velocity variability. Vertical bars in (a and c) indicate times of potential offsets for equipment (magenta) and earthquake (gray) events. Red lines in (a and c) are models of the time series that include parameters for intercept, trend, Heaviside steps at equipment and earthquake steps, and annual, and semiannual seasonal terms. The green horizontal lines in (b and d) indicate the MIDAS velocity (solid) and ±MAD of the velocity time series (dotted). Note that the difference in vertical axis scale between (b and d).

these clusters, this nearest neighbor variability is a measure of noise that is mitigated by the spatial filtering. Here, we quantify this spatial variability and show it has very weak dependence on the temporal variability, which indicates that it must be separately accounted for when assessing the quality of VLM estimate.

We define the nearest neighbor spatial variability ζ_i at station i as the MAD of the rates at neighboring stations that are connected to i by Delaunay triangulation:

$$\zeta_i = \text{MAD}\left(v_k\right) \tag{9}$$

This kind of spatial variability is strongly affected by interstation separation distance and is expected to be noise that is very different in structure compared to the signals encoded in the *ssf* which is estimated
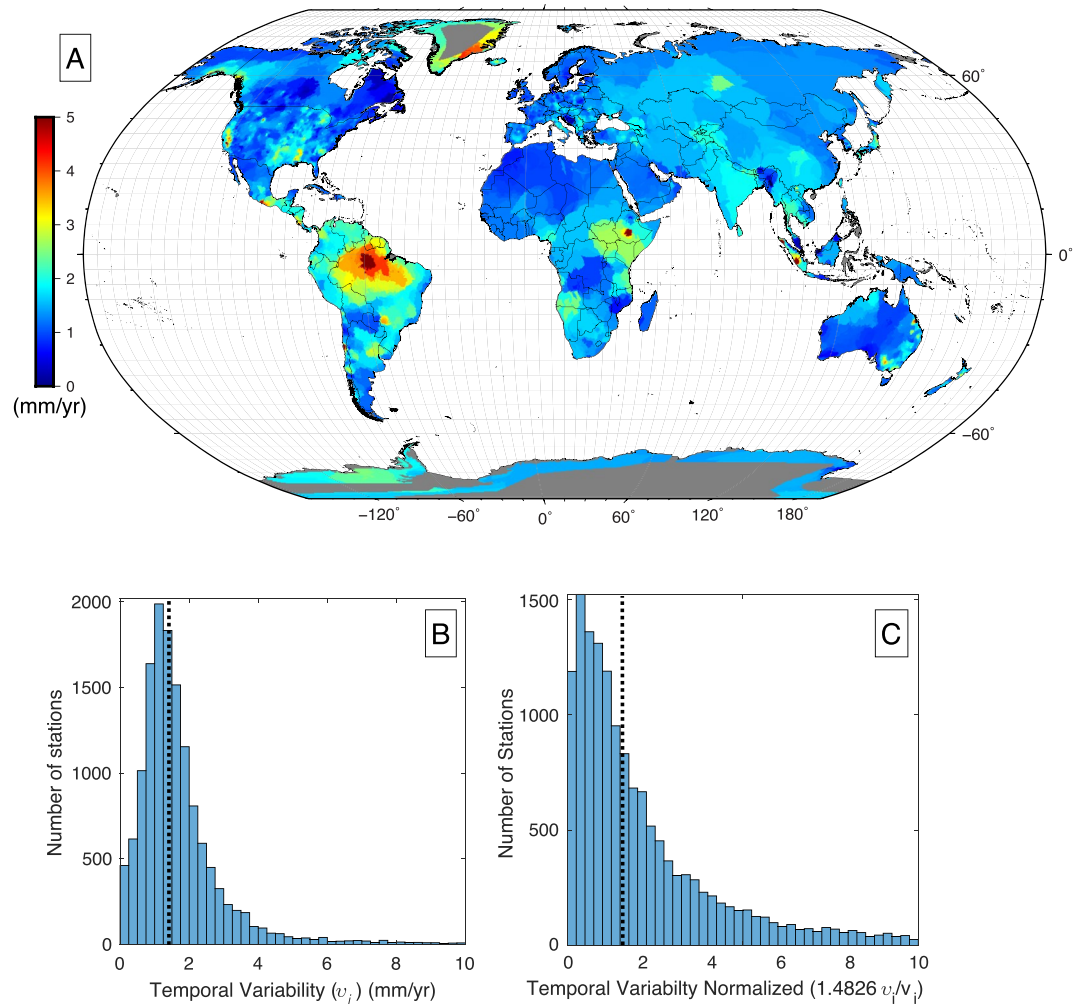
Figure 7. (a) GPS Imaging of nonseasonal vertical velocity variability ($\hat{v}_j$) on land areas. Red areas have high variability, blue low. (b) Histogram of variability at stations v_i, vertical dotted line indicates median value. (c) Histogram of variability at stations v_i, normalized by the vertical rate at the station v_i.

from rates from stations separated by large distances. Figure 8 shows the relationship between ζ_i and v_i in a scatterplot of the values in a logarithmic scale. The plot shows that there is a relatively weak correlation ($r = 0.240$) between the $\log_{10}(\zeta_i)$ and $\log_{10}(v_i)$. The correlation between ζ_i and v_i is even weaker ($r = 0.028$). Thus, the spatial and temporal variabilities are generally distinct and separate indicators of noise contributions, and both should be considered when evaluating the reliability of GPS-based estimates of VLM trends. Below, we show an example of how to use the variabilities as a tool for diagnosing the source of VLM uncertainty, showing how reliability of rates can be evaluated.

3.6. Summary of Uncertainty Factors

The uncertainty components have symmetries (summarized in Table 1) that we note in an attempt to make them easier to understand and remember. We distinguish the sources of uncertainty as temporal (σ, v) or spatial (ζ, η) in origins, and also whether the uncertainty is aleatory, that is, estimated from the scatter around the estimated value (σ, ζ) or from signal variability in the (spatial or temporal) neighborhood in which the estimate is made (η, v). We distinguish signals at GPS stations (e.g., v_i) from signals imaged from multiple stations with a carat (e.g., $\hat{v}_j$).
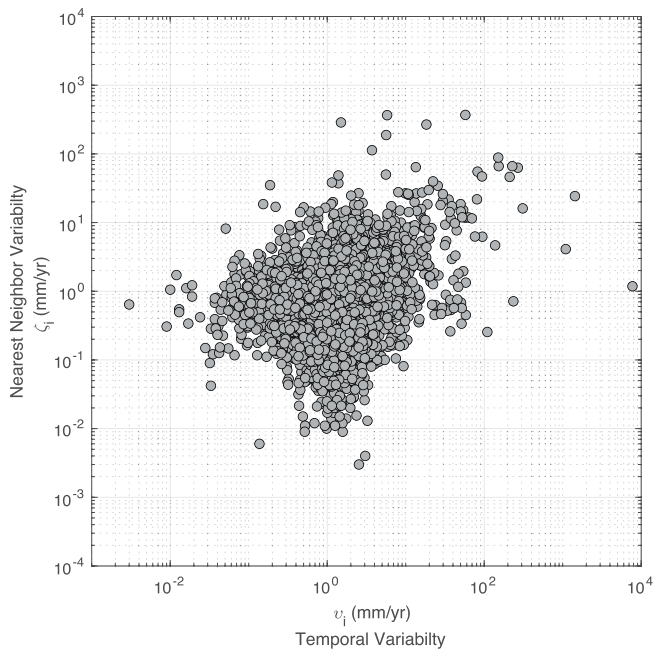
Figure 8. Independence of v_i and ζ_i from one another is shown in this scatter plot of temporal rate variability v_i versus nearest neighbor spatial variability ζ_i.

Having these defined clarifies the sources of uncertainty in VLM at specific locations. As an example, we consider the tide gauge in San Francisco, CA (longitude −122.465°, latitude 37.807°). The constraints on VLM at this location are given in Table 2. The table lists the GPS stations that contribute to the estimate of $\hat{v}_j$ (imaged GPS rate at the tide gauge location), including the important values that characterize the rate and uncertainty. In this case, the five stations (CADY, CCSF, MDHL, PBL1, and UCSF) have rate uncertainties that vary from 0.61 to 0.95 mm year^{-1}. The stations are all relatively close to the tide gauge compared to the wavelength of the signal, as indicated by $\eta_i = 0.913$ for all stations, with the closest station (MHDL) having $\eta_i = 0.938$. The stations contribute with slightly different weights (varying from 0.172 to 0.268) to the median value of $\hat{v}_j = -0.64$ mm year^{-1}. Nearest neighbor variability $\hat{\zeta}_j$ and temporal variability $\hat{v}_j$ are in the middle of the ranges for these parameters (Figures 7 and 8). Thus, the overall estimate of VLM is typically well constrained at the San Francisco tide gauge, since the contributing uncertainties are near the middle of their ranges. Below, we illustrate with an example where the VLM estimates at the tide gauges are ranked in quality.

4. Results

We show the result of GPS Imaging the vertical rates with the oceanic areas masked out because coverage in the ocean basins is generally poor (Figure 9). We do not exclude stations on islands in the ocean basins from the analysis but mask out the resulting estimate of the vertical rate field. Thus, stations on islands near the coast can contribute if they are close enough to have a significant weight. In this section, we discuss some features of the signals, recognizing that some have been described previously, others not. While a complete discussion of all aspects of VLM on Earth is beyond the scope of what is possible to cover in this manuscript, we point out some important features of the rate field. In Discussion, we discuss the global balance of vertical motion across the Earth's surface, and how much of this motion is attributable to non-GIA sources.

4.1. GIA

Immediately clear and of greatest impact are the GIA uplift signals of Fennoscandia in Northern Europe, northern North America, and Antarctica that have been documented in many previous studies (reviewed in Whitehouse (2018)). These signals have been measured extensively using multiple techniques, including GPS, leveling, gravity, raised shorelines, and tide gauges, and dominate the uplift field with maximum values over 10 mm year^{-1} that span thousands of kilometers. VLM from GIA also includes large areas undergo-

Table 1
Components of GPS Imaging Uncertainty

Value at station	Imaged value	Unit	Description
v_i	$\hat{v}_j$	mm year^{-1}	MIDAS rate at station and imaged MIDAS rate at evaluation point
σ_i	$\hat{\sigma}_j$	mm year^{-1}	Aleatory MIDAS rate uncertainty and uncertainty of imaged rate at evaluation point j
η_i	$\hat{\eta}_j$	unitless [0,1]	Median *ssf* value from distances to stations used in imaging rate
ζ_i	$\hat{\zeta}_j$	mm year^{-1}	Nearest neighbor scatter (MAD) of MIDAS rates around station or around grid point
v_i	$\hat{v}_j$	mm year^{-1}	Temporal variability (MAD) of rate at station from time series

Table 2
Example Imaging Result of VLM Rate at Tide Gauge in San Francisco, California

San Francisco, CA	Lon.	Lat.	$\hat{v}_j$	$\hat{\sigma}_j$	$\hat{\eta}_j$	$\hat{\zeta}_j$	$\hat{\upsilon}_j$
	−122.465	37.807	−0.641	0.354	0.913	0.539	1.441
Contributing GPS station	v_i (mm year^{-1})	v_i (filtered)	σ_i (mm year^{-1})	Δ_{ij} (km)	η_i	v_i (mm year^{-1})	w'_i
CADY	−0.595	−0.927	0.845	9.43	0.883	1.177	0.181
CCSF	−1.937	−1.354	0.826	8.58	0.888	1.328	0.187
MHDL	−0.639	−0.641	0.946	4.72	0.938	3.144	0.172
PBL1	−0.100	−0.641	0.824	6.56	0.913	1.441	0.192
UCSF	−1.477	−0.639	0.606	4.89	0.936	2.272	0.268

ing fore-bulge collapse, including the northern midwest to east coast regions of the United States, northern Alaska, and southern Europe. Areas of high GIA rates often have very low seasonal and nonseason velocity variability (Figures 5 and 7) consistent with the processes being a long-term steady feature of mantle flow.

4.2. Non-GIA-Related VLM

4.2.1. Subduction Zones

Coastal areas at convergent tectonic plate boundaries experience vertical motions associated with interseismic strain accumulation at subduction zones. The islands of Japan and Sumatra are heavily affected and have high degrees of velocity variability (Figure 7) indicating effects from their high rate of recent seismic activity. While $\hat{v}$ is insensitive to the coseismic steps themselves, these events initiate postseismic mantle relaxation which cause vertical velocities to evolve over months to decades (e.g., Pollitz et al., 2006; Yamagiwa et al., 2014). The Nazca subduction zone in South America exhibits the Earth's longest section of onshore interseismic uplift that is nearly continuous from southern Chile to southern Peru (Figure 9). At the northern end of this zone, the imaging of interseismic uplift becomes equivocal in Peru where there are fewer coastal GPS stations available and also exhibits a medium degrees of velocity variability in the stations that do exist (Figure 7). At this latitude, horizontal GPS measurements indicate that the degree of coupling of the plate interface undergoes a transition from locked to creeping (Chlieh et al., 2011), so onshore uplift may not extend further north. In the Cascadia subduction zone of the Pacific Northwest of the United States, we also see interseismic uplift. However, it is difficult to see in a map of the scale of Figure 9, especially since the uplift occurs only near the southern and northern ends of Cascadia, where the trench is close enough to
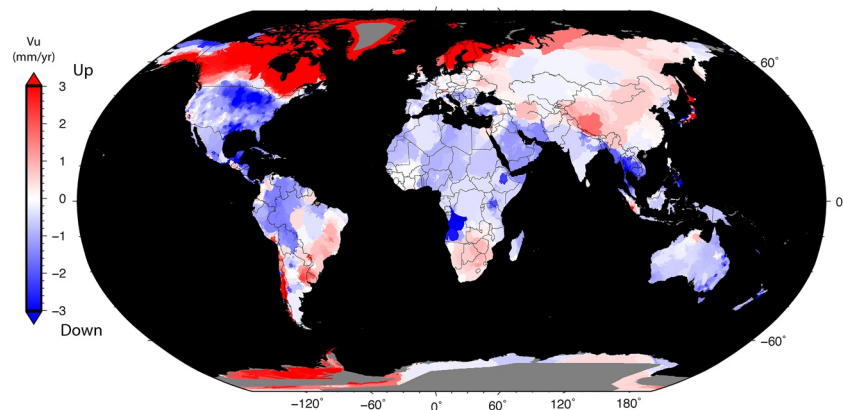

Figure 9. GPS Imaging of vertical rate on land areas, blue is downward, red upward.

drive onshore uplift (Burgette et al., 2009; Mazzotti et al., 2007). Velocity variability of Cascadia coastal GPS stations is generally low, consistent with steady uplift and the lack of recent slip of the megathrust.

Coastal subduction-related uplift or subsidence may, according to our GPS measurement of VLM variability, appear steady. However, it is transient when considering time scales longer than the seismic cycles, for example, ~500 years in Cascadia (Atwater & Hemphill-Haley, 1997), when earthquakes reset the cycle so that areas with net uplift will subside and vice versa. Thus in these cases, projections of sea level rise over time scales longer that the period of GPS observation would be misled by the GPS rates, which should be considered as valid until the time of the next large earthquake.

4.2.2. The Amazon Basin

The Amazon Basin has been shown with GPS and GRACE data to experience very large seasonal fluctuations in vertical and horizontal motions (Ferreira et al., 2020; Fu et al., 2013). We find, in addition to the large seasonality of vertical motion, a very high degree of nonseasonal uplift rate variability, the largest and most variable on Earth in the imaging with the greatest variability located at the Amazon River (Figure 6). This indicates that changes in rates in the Amazon not only are seasonal but also have trends that inflect upward and downward, changing sign on multiannual time scales between drought and wet periods. This may explain why when considering overall trends Knowles et al. (2020) found an uplift trend in the Amazon, while our results show a combination of uplift and subsidence. This is consistent with the imaged temporal variability and indicates that the trends in the Amazon Basin are likely not permanent features of the vertical GPS rate field, and the sign of uplift depends on the time period of observation.

4.2.3. Australia

In Australia, uplift rates change in sign depending on the time interval observed. Han (2017), for example, found that the Australian continent was depressed by the La Niña water load in 2010–2011 and afterward rebounded as the water load evaporated. When considering the overall trends, however, we find mostly subsidence in Australia over our period of observation, where the median value of the image is -0.8 mm year^{-1}, and 97.8% of the pixels in the image have negative vertical rate. There is low variability in the central and western part of the country and moderate variability on the eastern part of the country, consistent with some impact from the climate-related loading sources. Nearly, all Australia subsides (with the exception of a patch of the Northern Territory) but the trend is likely not a long-term effect. Also, these rates have been shown to be inconsistent with the effects of GIA (Riddell et al., 2020), and the moderate variability suggests a time-variable source, which is also inconsistent with GIA. Riddell et al. (2020) also discussed numerous potential noise sources that could result in a downward trend for all of Australia, including biases in GPS from draconitic period signals, reference frame origin and geocenter drift, colored noise, but did not settle on single likely source. If the land surface in Australia continues to subside at the imaged rate most of Australia, which is the lowest continental land mass in the world, would be submerged in half a million years. This is not likely to happen since similar subsidence has not occurred in the recent geological past (Sandiford, 2007). However, subsidence over the time scale of the glacial cycles would not continue as long and may be feasible. If VLM oscillated with periods longer than observed with GPS, then the GPS data would not be sensitive to this variability. GRACE data indicate that the western half of Australia has experienced steady loss in equivalent water height in 2003–2016, while the eastern half experienced mass gain (Luthcke et al., 2013; Watkins et al., 2015) suggesting the continent-wide subsidence is not a single process related to hydrological loading or poroelastic deformation. Given that GRACE and vertical rate variability differ, it may be that the imaged subsidence is driven by different factors in the west and east halves of Australia.

4.2.4. Southwest Africa

The GPS network in Angola has 16 stations, almost all of which provided data for the same interval, from 2010 to 2015. During that time nearly all of the stations experienced subsidence at rates between 2 and 6 mm year^{-1} and are responsible for the subsiding area in southwest Africa (Figure 9). Hydrogeology data for Angola indicate the presence of a group of large moderate-to-high productivity aquifer systems in unconsolidated and Tertiary-Quaternary sediments (Africa Groundwater Atlas, 2020; MacDonald et al., 2012). While the GPS data consistently indicate subsidence, they are geographically sparse and have near the minimum of completeness and duration we allow in our analysis. Their median completeness is 31%, that is, on average

116 days of observation per year, which should be enough to prevent bias in the estimate of the rate and its variability. The temporal variability is moderate in this part of Africa (Figure 7) further suggesting that the aquifer affects vertical motions. Observations of trends in GRACE data from 2010 to 2015 in mascons in Angola indicate a complex time series of water equivalent height changes that increase and decrease over time but have a general decrease over these years. Decrease in overall water mass associated with surface subsidence and high temporal GPS rate variability is all consistent with the effects of porous aquifer depletion. Similar signals of subsidence and mass loss at other locations have been attributed to aquifer depletion and compaction, for example, in the California Central Valley (Famiglietti et al., 2011; Faunt, 2009).

4.2.5. Southern Africa

In Southern Africa, there is a spatially coherent anomaly with peak uplift rate of about 1 mm year^{-1} in the northern part of the country of South Africa, southern Zimbabwe, and eastern Botswana. The amplitude of uplift decreases toward the coastline on both east and west coasts of South Africa. The anomaly is well imaged by the network, with 79 stations having a median observation duration of 13.4 years. The neighboring countries of Namibia, Botswana, Zimbabwe, and Mozambique have fewer stations in the NGL database, with between 0 and 10 stations in each country, so constraints on VLM are not as strong. The East Africa Rift (EAR) has many GPS stations but does not show an uplift anomaly. The transition between upward and downward moving domains lies along the EAR plate boundary where it trends along Lakes Tanganyika and Malawi toward the Indian Ocean. This zone is the extensional boundary between the Rovuma microplate and the Nubian plate (Saria et al., 2013; Stamps et al., 2018). At this boundary, the extensional EAR gives way southward to the Kalihari Craton, where the lithosphere and sublithospheric mantle have faster seismic velocities (Paysanos & Nyblade, 2007) indicating it is a major transition in lithospheric structure across the Rift.

South of the EAR, within the uplift domain, Figure 7 shows low to medium levels of temporal variability, but to the north of the EAR variability is higher. This suggests that the EAR may be affected by climate-related uplift signals that are not sufficient to drive uplift trends. Trends in equivalent water thickness from GRACE in South Africa and the EAR are mixed in sign, including signals of both increasing and decreasing anomalies in equivalent water height. Thus, spatially the VLM trends are not consistent with the mass change trends, suggesting that the uplift anomaly is not a consequence of mass unloading from climate-related or hydrological loading effects. While the uplift domain has proximity to the aquifer-driven subsidence in Angola (discussed in Section 4.2.4.), it does not surround the zone of subsidence and therefore does not have the spatial characteristics of an unloading feature from water loss centered on the Angola aquifers. However, GPS constraints to the north and northwest of Angola are poor to nonexistent, so a radially symmetric uplift zone could be present but is not detected.

The large size, regional coherence, and low variability of the uplift anomaly in southern Africa indicate that it may be a geodynamic consequence of mantle flow, dynamic topography, and/or lithosphere-scale processes. The location of this uplift domain south of the EAR plate boundary corresponds to a part of the broad region of high elevations and shallow bathymetry termed the south African Superswell (Nyblade & Robinson, 1994). Support of the Superswell has been attributed to buoyancy and consequent vertical flow in the mantle as derived from seismic velocity anomalies (Lithgow-Bertelloni & Silver, 1998). While the exact locus in the mantle of where the support originates, that is, whether primarily from the deep lower mantle low seismic velocity zone or shallower upper mantle features, has not be conclusively determined (Gilfillan et al., 2019), it is roughly collocated with the current location of the Quathlamba hotspot and plume (Hartnady, 1985) suggesting a connection. However, the coincidence of the boundary between uplift and subsidence with the southern EAR suggests a component that could be influenced by shallower lithospheric processes, and thus the entire effect may result from an interaction between asthenospheric mantle flow and surface plate kinematics. But in any case, this class of explanation implies that the uplift is a persistent feature and that the VLM will be a steady contribution that should be accounted for in sea level rise projections for southern Africa.

4.2.6. The Himalaya and Asia

The high mountain region of the Himalayan Mountain chain was built in response to collision between the Indian subcontinent and Asia, and this is evident in its active uplift (Avouac, 2003). This region is not near coasts where sea level rise is a concern, so we do not discuss these signals at length. However, the smearing
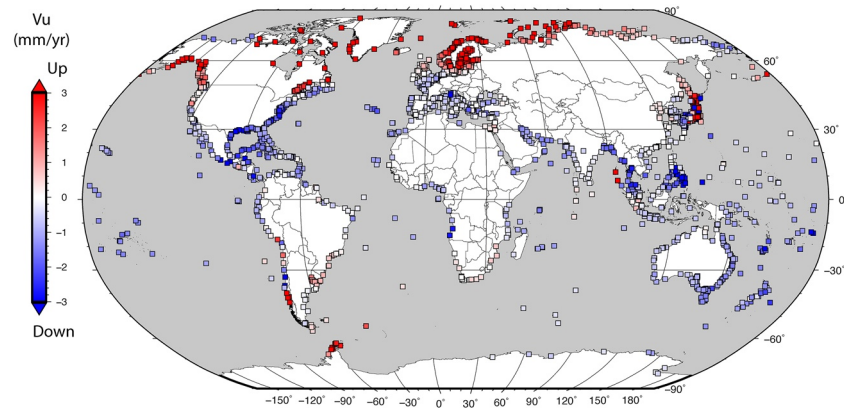
Figure 10. Vertical rates at tide gauges of the Permanent Service for Global Mean Sea Level (Holgate et al., 2013). See Supplementary Table S1 for rates at each tide gauge along with list of GPS stations that contributed to the rate and associated temporal and spatial uncertainty parameters.

of these signals is among the most extreme on Earth so bears a brief discussion since it illustrates how GPS Imaging behaves when station density is highly variable. In general, GPS Imaging exhibits no preference for zero rates, that is, the image is in no way biased toward zero, so areas with poor coverage tend to take on signals from nearby measured areas. In China, for example, there are very few GPS stations in the NGL database but there are many on its periphery. Thus, the imaged uplift is largely a function of stations outside China. There are enough stations in Nepal (which has a higher η_j, Figure 4) so that the uplift is adequately separated from the signal of subsidence in India (Fu & Freymueller, 2012). Thus, smearing from Nepal is mostly to the northeast into China and south into India.

4.3. VLM at Tide Gauges

Although changes in global mean sea surface height are important for understanding the impacts of sea level rise at coasts (Church & White, 2011; Milne et al., 2009), it is the change in sea level relative to the land (RSL) that is, most relevant. Networks of tide gauges provide the most widely used way to measure RSL (e.g., Church et al., 2004; Davis & Mitrovica, 1996; Douglas, 2001; Pugh & Woodworth, 2014). However, tide gauge measurements are affected by movement of the land and of the sea surface, leaving the driving factor behind RSL ambiguous. Sea surface altimetry, which has global coverage, can be used to assess the relationship between RSL and VLM (e.g., Cazenave et al., 1999; Nerem & Mitchum, 2002; Ray et al., 2010) but connecting open ocean sea height measurements to the coast can be challenging (Wise et al., 2018). Regional VLM measurements can be combined with tide gauge and satellite altimetry to better reconcile the budget related to RSL changes by combining all three techniques (e.g., Hawkins et al., 2019). In any case, improving knowledge of VLM at the tide gauges is critical for reconciling the various constraints on RSL and its impact on coastal communities.

Here, we estimate the rate of VLM at the 2,357 tide gauge stations of the Permanent Service for Global Mean Sea Level (PSMSL, Holgate et al., 2013) using GPS Imaging. The estimation points are the tide gauge coordinates instead of the regular grid points used in the GPS Imaging and include locations on islands in the ocean basins (Figure 10). The patterns of VLM at the tide gauges follow those seen in the individual GPS stations and in the imaging (Figures 1 and 9). Subtracting the rates of VLM from the rates of sea level rise estimated from tide gauges tends to increase the mean rate of sea level rise by 0.2–0.3 mm year^{-1} (Figure 11) because of the concentration of tide gauges in areas with positive VLM. This remains true whether considering the entire set of the tide gauge data, only data from 1993 to the present, or only data from 2000 to the present. The increase in rate of sea level rise owing to the VLM correction is less than the increase of rate that has occurred in recent decades owing to climate change (Nerem et al., 2018).

The uncertainty of the GPS VLM rate at the tide gauges is a function of the data at the nearest GPS stations, including their number, distance, uncertainty, and variability of their trend estimates. These are given by its uncertainty vector ($\hat{\sigma}_j, \hat{\eta}_j, \hat{\zeta}_j, \hat{\upsilon}_j$) as described in Table 1. Supplementary Table S1 presents a data record
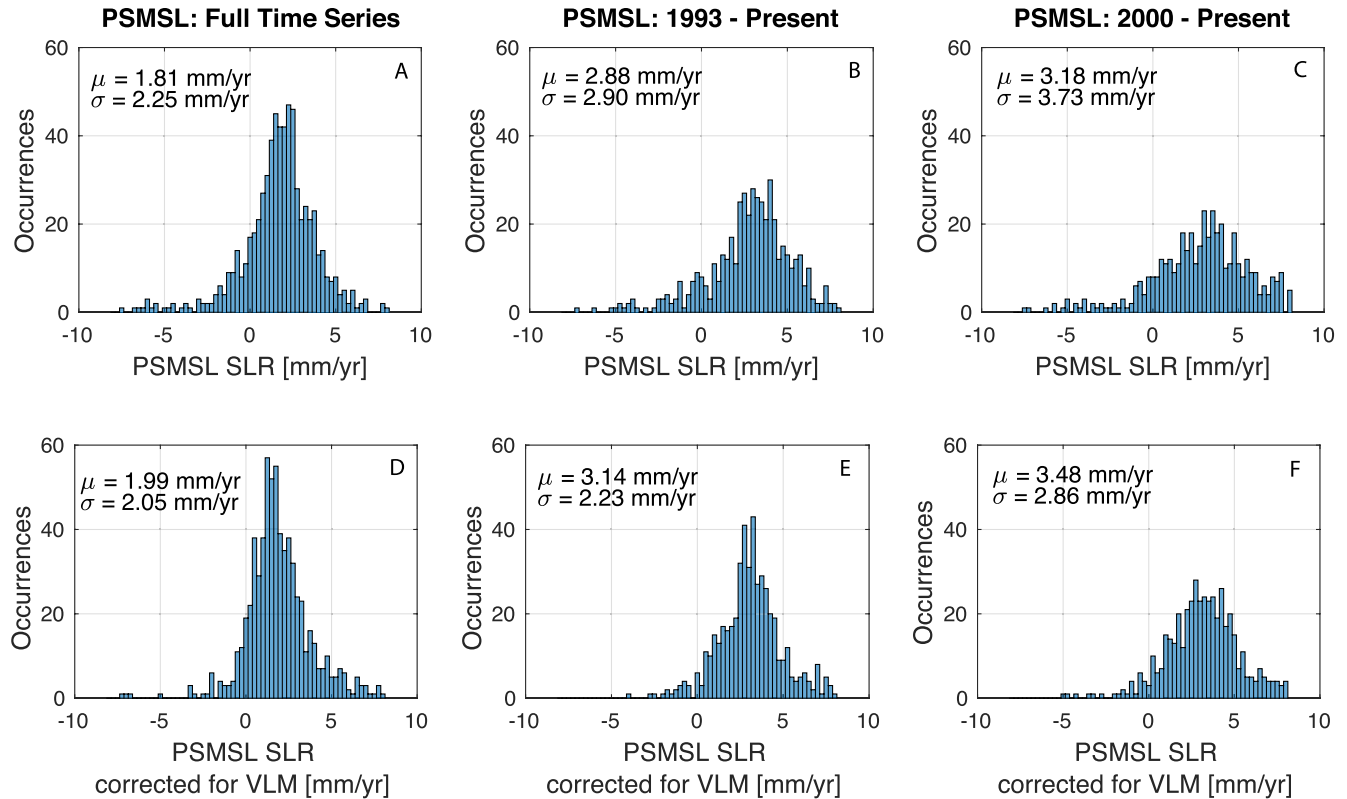
Figure 11. Histograms of the rate of relative sea level rise from tide gauges in the holdings of the Permanent Service for Global Mean Sea Level (with outliers removed) given for (a) all times available from the time series, (b) data from 1993 to present, and (c) from 2000 to present. The lower row (d–f) show the same histograms except for sea level rise trends adjusted for VLM shown in Figure 10.

for each tide gauge with the same information as in Table 2, so that the uncertainty may be assessed. The completeness of this table allows it to be used in subsequent analysis to objectively rank order tide gauges by VLM quality constraints and provides a means to trace back to which sources of uncertainty are most important for a given gauge. Exactly which uncertainty components are most important depends on the goals of a subsequent analysis. For example, in some cases, low temporal variability stations may be required or in others low spatial variability.

We provide an example approach where the tide gauges are rank ordered according to quality constraints, that is, which have good, medium, or poor quality VLM estimates. We use a balanced set of criteria based on the distributions of the four kinds of uncertainty. Figure 12 shows a histogram of each uncertainty parameter, with vertical bars that indicate how each parameter is divided into its tercile ranges (lowest, middle, and highest thirds of the data) and the 5th and 95th percentile ranges. We consider a VLM constraint at a tide gauge "good" if it *none* of its uncertainty measures lies in the worst tercile. This corresponds to the condition $\hat{\sigma} < 0.42$ mm year^{-1}, $\hat{\zeta} < 0.86$ mm year^{-1}, $\hat{\upsilon} < 1.54$ mm year^{-1}, and $\hat{\eta} > 0.57$. In this case, the 33.1% of the tide gauges fall into this "good" category. We call a VLM constraint "poor" if *any* of its uncertainty parameters $\hat{\sigma}$, $\hat{\zeta}$, $\hat{\upsilon}$, $\hat{\eta}$ are in the 95% percentile, that is, among the worst 5% of the values. In this case, the 15.5% of the tide gauges fall into this "poor" category. The remaining tide gauges have medium quality, and these comprise 51.4% of the gauges. Figure 13 shows the locations of the gauges with good, medium, and poor constraints. VLM tends to be well constrained (mostly "good") at gauges where GPS networks are dense, but this is not always the case. For example, in California, there are 26 tide gauges in the PMSL, 13 of which have "good" VLM constraint and 13 have "medium" constraint. In Japan, despite the excellent coverage with GPS, about 33% of gauges have "poor" VLM constraint. None of the tide gauges with "poor" VLM constraints are classified as such because of a low $\hat{\eta}$, consistent with the excellent geographic coverage of GPS networks in Japan. About two thirds of these are classified as "poor" because they exceed the threshold
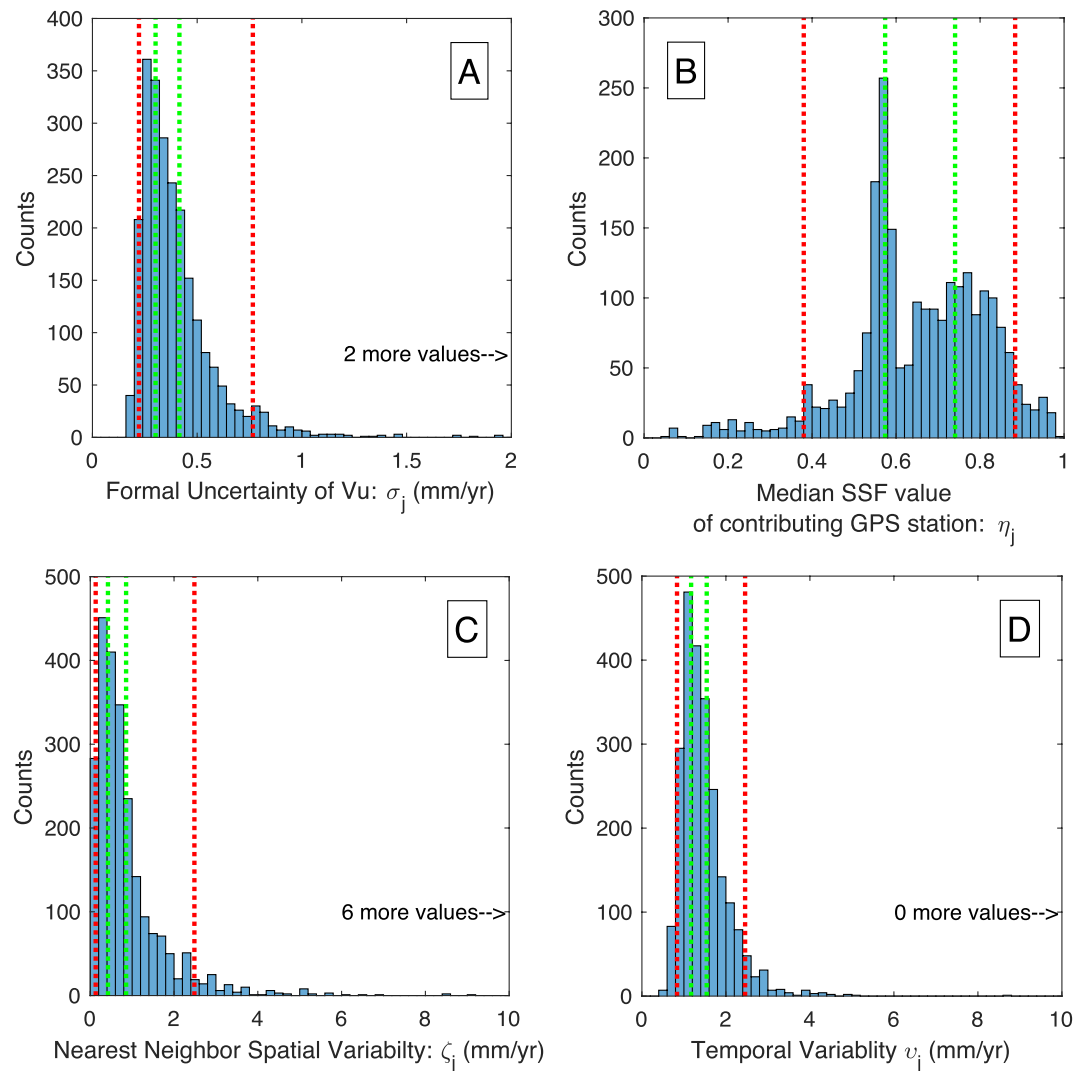
Figure 12. Histograms of the uncertainty parameters of GPS Imaged vertical land motion (VLM) rates at tide gauge locations. (a) MIDAS rate uncertainty $\hat{\sigma}_j$, (b) *ssf* value at distance to nearest GPS station $\hat{\eta}_j$, (c) nearest neighbor variability $\hat{\zeta}_j$, and (d) temporal rate variability $\hat{\upsilon}_j$. Vertical bars indicate terciles separating lower, middle, and upper third of data (green dashed lines) and limits of 5% and 95% percentiles of the data (red dashed lines). These are used to divide tide gauge stations into sets with good, medium, and poor GPS estimates of VLM (see Figure 12 and text for discussion).

for temporal rate variability ($\hat{\upsilon}$), consistent with the seismic cycle in Japan causing large changes in uplift rates over the observed time.

5. Discussion: Integrating Global VLM Constraints

A benefit of GPS Imaging is that it balances the contributions from stations that are very heterogeneously distributed. For example, the median vertical rate of the GPS stations is -0.60 mm year^{-1}, a value that is, significantly different than zero given the large number of data used to estimate it. However, this signal reflects the number of stations that are concentrated in areas that experience subsidence, for example, the large fraction of the central United States that undergoes fore-bulge collapse (Figure 1). While uncertainties in the imaged field (Figure 9) are not the same everywhere, it does represent a field that is, geographically balanced and can be used to evaluate properties of Earth's global VLM field. Some recent studies have provided global-scale interpolated VLM based on the NGL database (e.g., Husson et al., 2018; Schumacher
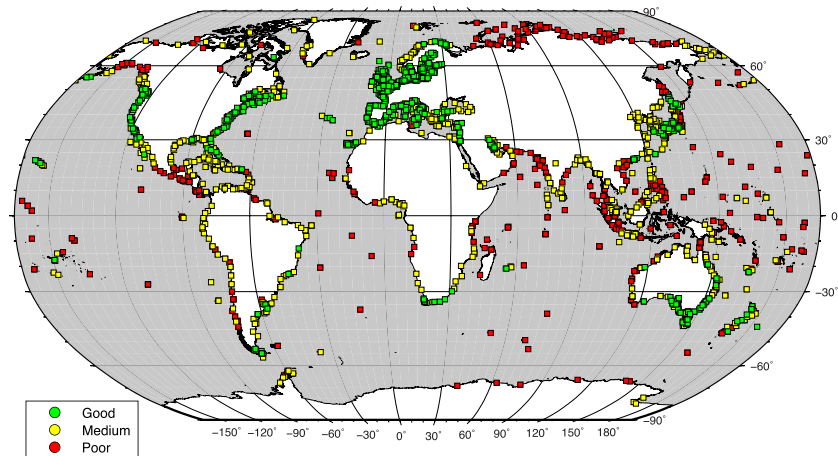
Figure 13. Map indicating by color whether vertical land motion estimate at tide gauge location is good (green), medium (yellow), or poor (red) according to criteria discussed in text.

et al., 2018) but tend to focus their concern on the GIA process. Detailed comparison of results from the GPS Imaging and Bayesian surface reconstruction methods has been conducted elsewhere (Husson et al., 2018) so we do not repeat such comparisons here.

We wish to assess the impact of non-GIA so we ask the questions: how much of the global VLM is non-GIA-related? and how significant is it on a global scale? To do this, we first quantify the impact of the VLM field by integrating to estimate vertical volume flux rate:

$$\dot{F} = \int_{\partial S} \hat{v}(\vec{r}) dA \tag{10}$$

where $\vec{r}$ denotes position and ∂S can be any part or all of Earth's surface. This kinematic formula is valid regardless of the driving process behind the VLM, be it tectonics, GIA, elastic loading, viscoelastic flow, poroelastic rebound, etc. If the volume encapsulated by the entire Earth's surface is constant over time, then $\dot{F} = 0$ when ∂S covers all of Earth. Several of the most important processes driving VLM are conserving in this way. For example, mantle flow and surface loading are $\dot{F} = 0$ since the loads on Earth surface move from place to place and never leave Earth. Integrating the ICE-6G_C GIA model (Argus et al., 2014; Peltier et al., 2015) results in total $\dot{F} \sim 0$. This means that while GIA currently drives uplift in some places, elsewhere it is matched by subsidence to keep the Earth volume constant. Similarly, hydrological loading changes are net $\dot{F} = 0$, since water moving of the surface changes a load location, but the net deflection is the same. The same is true for some other processes but not all. For example, water that is, removed from an aquifer will cause a change in loading location, but also causes a separate contribution to subsidence owing to compaction and/or poroelasticity. The poroelastic effect is not volume conserving because the water does not necessarily return to another aquifer, resulting in net subsidence. Thus, the total Earth surface is not strictly volume conserving but is approximately so since the largest mechanisms are GIA and hydrological loading, and others have relatively minor effects.

When we perform the integration in Equation 10 over Earth's land areas, we find that the net vertical volume flux of the observed land areas is 22.1 km^3 year^{-1} (Table 3). The land areas are in net uplift, implying that the unobserved areas (e.g., ocean basins and masked areas under existing ice sheets) experience net subsidence. Averaged over the observed land area the net uplift is 0.16 mm year^{-1}, while the subsidence in the unobserved areas needed to compensate is −0.06 mm year^{-1}, a slower absolute rate because the unobserved areas have a larger area.

But how much of this is attributable to non-GIA processes? We can begin to address this by correcting the VLM field using a GIA model. The GIA model we consider (ICE-6G_C—Argus et al., 2014; Peltier et al., 2015) has a net upward vertical flux in the imaged land areas of 87.5 km^3 year^{-1} and downward flux of −13.7 km^3 year^{-1} for a net upward flux of 73.8 km^3 year^{-1} (Table 3). The net flux of the GIA model is far greater than the net

Table 3
Vertical Volume Flux Rate of Earth's Major Land Masses

Land mass	% of total	Flux GPS Imaging			Flux GIA model ICE-6G			Residual (non-GIA VLM)		
		Total	Positive	Negative	Total	Positive	Negative	Total	Positive	Negative
		(km^3 year^{-1})			(km^3 year^{-1})			(km^3 year^{-1})		
Eurasia	9.88	5.1	18.8	−13.8	22.2	22.9	−0.7	−17.1	−4.0	−13.1
Africa	5.76	−15.3	2.5	−17.8	−0.4	0.7	−1.2	−14.9	1.8	−16.6
N. America	3.93	20.3	36.5	−16.2	31.1	41.4	−10.3	−10.8	−5.0	−5.8
S. America	3.44	−1.5	7.0	−8.5	4.0	4.2	−0.2	−5.5	2.8	−8.3
Antarctica	2.36	8.6	9.4	−0.8	13.0	13.2	−0.2	−4.4	−3.7	−0.7
Australia	1.49	−5.0	0.1	−5.1	−0.8	0.0	−0.8	−4.2	0.1	−4.3
Greenland	0.40	8.1	8.1	0.0	1.9	2.2	−0.3	6.2	6.0	0.3
New Guinea	0.15	−0.9	0.0	−0.9	0.1	0.1	0.0	−1.0	−0.1	−0.9
Borneo	0.15	−0.4	0.0	−0.4	0.2	0.2	0.0	−0.5	−0.2	−0.4
Madagascar	0.12	−0.3	0.0	−0.3	0.0	0.0	0.0	−0.4	0.0	−0.3
Baffin Island	0.09	2.6	2.6	0.0	2.2	2.2	0.0	0.4	0.4	0.0
Sumatra	0.08	0.4	0.4	−0.1	0.1	0.1	0.0	0.3	0.4	−0.1
Honshu	0.04	0.6	0.8	−0.2	0.1	0.1	0.0	0.5	0.7	−0.2
Great Britain	0.04	0.0	0.1	−0.1	0.1	0.1	0.0	0.0	0.0	0.0
New Zealand	0.03	−0.3	0.0	−0.4	0.0	0.0	0.0	−0.4	0.0	−0.4
Total	27.96	22.1	86.5	−64.5	73.8	87.5	−13.7	−51.7	−1.0	−50.7

Abbreviations: GIA, glacial isostatic adjustment; VLM, vertical land motion.

22.1 km^3 year^{-1} found in the imaging of the same land area, suggesting that non-GIA processes drive net subsidence on the continents. Subtracting the predictions of the GIA model from the VLM field (Figure 9) removes most of the uplift and fore-bulge subsidence in North America and Europe and changes signals in Antarctica (Figure 14). The residual volume flux of −51.7 km^3 year^{-1} is the strongly negative (downward) net signal that non-GIA vertical motion has on the land areas. That these trends are largely caused by elastic response of the Earth to changes in the location of hydrological loading is evident when comparing the VLM trends to trends in GRACE data. Figure 14 shows the trends from GRACE, with the scale flipped so that drying is portrayed as red so it may be compared to locations where GPS-measured motion is upward, and blue can be compared to locations where GPS-measured motion is downward, consistent with loading. While differences in GPS and GRACE resolution exist, in many locations there are similarities between GRACE and GPS signals which are consistent with the effects of elastic hydrological loading, just as they were similar in their seasonality (Figure 5). In many areas, the GPS and GRACE trends do not agree, suggesting processes other than GIA or hydrological loading (e.g., tectonics, mantle flow, aquifer dynamics) drive trends in VLM. Also, disagreements between GPS and GRACE seem to be in the areas that are not well covered by GPS. Clearly, having a global model for time-variable hydrological elastic loading to correct the GPS and GRACE data is desirable, so we could evaluate these trends. Generating or evaluating such models is beyond the scope of this study, but progress is being made by several services that predict loading displacements globally using models of the atmosphere, oceans, and terrestrial hydrology, for example, those of the EOST/IPGS Loading Service (Mémin et al., 2020) and GFZ Earth System Modeling group (Dill & Dobslaw, 2013).

If non-GIA-related VLM observed on land is on balance negative, then this implies that much of the unobserved areas rise owing to non-GIA sources to maintain a near net-zero Earth volume (subject to the caveats mentioned above). This unobserved area includes the oceans and the currently ice-covered areas of Greenland and Antarctica, which over the period of observation with GPS have been losing mass at high rates owing to warming climate conditions with corresponding elastic unloading response that is not accounted for in the GIA model. Thus, it is likely that much of the uplift needed to balance the observed subsidence is under these
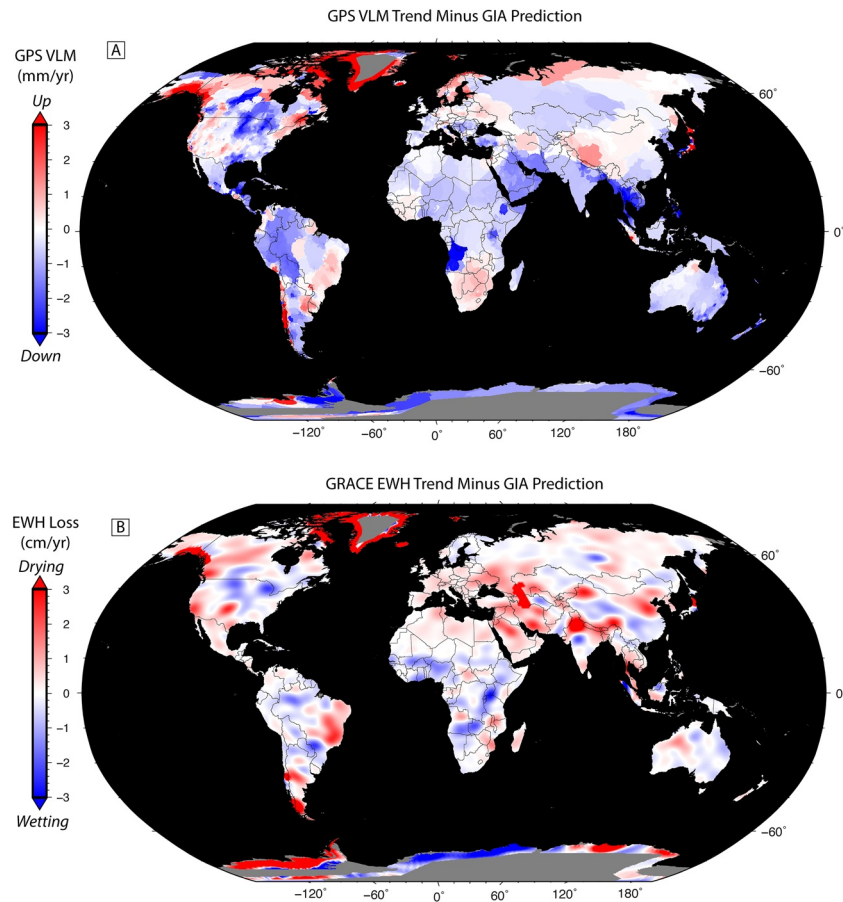
Figure 14. (a) The non-GIA VLM field estimated as in Figure 9 except with predictions of glacial isostatic adjustment (GIA) model (Argus et al., 2014; Peltier et al., 2015) subtracted. (b) Trends in equivalent water height from Gravity Recovery and Climate Experiment (GRACE) with the scale flipped so that water loss is reckoned positive. This results in a color scale that is red when GPS-measured motion is upward and GRACE indicates drying and is blue for GPS motion downward and increased GRACE-measured water load. Note that the GPS in is units of mm year^{-1} and GRACE in cm year^{-1}. This GRACE product is provided by Loomis et al. (2019) with the contribution from GIA removed.

ice sheets. It could also possible that the sea floor experiences net uplift owing to non-GIA-related processes. However, groundwater systems around the Earth are experiencing trends of depletion (e.g., Rodell et al., 2018) so a portion of the subsidence may be associated with aquifer compaction. Quantifying the proportion attributable to aquifer compaction will require more detailed study that includes comparisons with other data sets.

Regardless of the details in these arguments regarding budgets, the net volume flux of non-GIA VLM of -51.7 km^3 year^{-1} is nearly as great in absolute value as the GIA contribution of 73.8 km^3 year^{-1}. We conclude that while non-GIA VLM does not have as large an overall impact as GIA, it is still a globally substantial component of the total VLM, and it should be considered in analyses of RSL. This applies when correcting tide gauge records or closing the budgets between other techniques that measure trends in sea surface height such as satellite altimetry.

6. Conclusions

We use a database of vertical component position time series from globally distributed GPS stations to obtain a geographically balanced estimate of global VLM. The signals show a diversity of processes driving uplift and subsidence, including GIA, tectonic and seismic cycle deformation, seasonal and multiannual variations in hydrological loading, and many others. The imaged field is the observed VLM from all process-

es combined. Analysis of the net vertical flux from GPS Imaging averaged over the continents indicates that the non-GIA sources have about 70% of the impact of GIA's contribution to VLM.

Characteristics of the GPS signals help partition the sources of uncertainties in VLM, which are both spatial and temporal and come from aleatory uncertainty and signal variability. Considering all GPS stations in the database allows us to quantify these factors and summarize them for each tide gauge, providing the ability to identify sources of VLM uncertainty at each gauge. These results can be used to improve projections of present and future RSL rise from tide gauge and satellite altimetry data, which constrain RSL.

Comparison between GPS and GRACE data shows that most of the trends, seasonal changes, and multiannual variability in VLM come from interaction of Earth's surface with its fluid envelopes. Hydrological loading affects nearly all of Earth's surface.

VLM of the continents is on average upward, implying that the unobserved areas (composed of the ocean basins and areas currently under the large ice sheets) move on average downward with respect to Earth center. However, after correcting for GIA the reverse is true, and continents subside on average suggesting that the ocean basins and ice-sheet-covered areas undergo net non-GIA-related uplift. A large portion of this is likely attributable to elastic unloading from contemporary ice loss that is not accounted for in GIA models.

Data Availability Statement

The MIDAS velocity field and position time series used in this study were obtained from the Nevada Geodetic Laboratory (http://geodesy.unr.edu/velocities/midas.IGS14.txt). The original GPS data were processed using the GipsyX version 1.0 software and data products obtained from the Jet Propulsion Laboratory. The authors obtained the locations of the tide gauge stations from the Permanent Service for Mean Sea Level (https://www.psmsl.org). The GRACE mascon solutions were explored with the University of Colorado Center for Astrodynamics Research interactive online tool (https://ccar.colorado.edu/grace/index.html) and the mascon solutions were obtained from https://earth.gsfc.nasa.gov/geo/data/grace-mascons. The authors obtained the ICE-6G_C model predictions from the Center of Global Change Science (https://www.atmosp.physics.utoronto.ca/~peltier/data.php).

References

Adusumilli, S., Borsa, A. A., Fish, M. A., McMillan, H. K., & Silverii, F. (2019). A decade of water storage changes across the contiguous United States from GPS and satellite gravity. *Geophysical Research Letters*, *46*, 13006–13015. https://doi.org/10.1029/2019GL085370

Africa Groundwater Atlas. (2020). *Africa groundwater Atlas*. Retrieved from https://www2.bgs.ac.uk/africagroundwateratlas/index.cfm (accessed July 30, 2020).

Altamimi, Z., Rebischung, P., Métivier, L., & Collilieux, X. (2016). ITRF2014: A new release of the International Terrestrial Reference Frame modeling nonlinear station motions. *Journal of Geophysical Research: Solid Earth*, *121*, 6109–6131. https://doi.org/10.1002/2016JB013098

Amos, C. B., Audet, P., Hammond, W. C., Bürgmann, R., Johanson, I. A., & Blewitt, G. (2014). Uplift and seismicity driven by groundwater depletion in central California. *Nature*, *509*, 483–486. https://doi.org/10.1038/nature13275

Argus, D. F., Blewitt, G., Peltier, W. R., & Kreemer, C. (2011). Rise of the Ellsworth mountains and parts of the East Antarctic coast observed with GPS. *Geophysical Research Letters*, *38*, L16303. https://doi.org/10.1029/2011GL048025

Argus, D. F., Peltier, W. R., Drummond, R., & Moore, A. W. (2014). The Antarctica component of postglacial rebound model ICE-6G_C (VM5a) based upon GPS positioning, exposure age dating of ice thicknesses, and relative sea level histories. *Geophysical Journal International*, *198*, 537–563. https://doi.org/10.1093/gji/ggu140

Arnould, M., Coltice, N., Flament, N., Seigneur, V., & Müller, R. D. (2018). On the scales of dynamic topography in whole-mantle convection models. *Geochemistry, Geophysics, Geosystems*, *19*, 3140–3163. https://doi.org/10.1029/2018GC007516

Atwater, B. F., & Hemphill-Haley, E. (1997). Recurrence intervals for great earthquakes of the past 3500 years at northeastern Willapa Bay. *United States Geological Survey Professional Paper*, *1576*, 108.

Avouac, J. P. (2003). Mountain building, erosion, and the seismic cycle in the Nepal Himalaya. In *Advances in geophysics* (Vol. 46). San Diego, CA. Elsevier. https://doi.org/10.1016/s0065-2687(03)46001-9

Beavan, J., Denys, P., Denham, M., Hager, B., Herring, T., & Molnar, P. (2010). Distribution of present-day vertical deformation across the Southern Alps, New Zealand, from 10 years of GPS data. *Geophysical Research Letters*, *37*, L16305. https://doi.org/10.1029/2010GL044165

Bekaert, D. P. S., Hamlington, B., Buzzanga, B., & Jones, C. E. (2018). Spaceborne Synthetic Aperture Radar survey of subsidence in Hampton Roads, Virginia (USA). *Scientific Reports*, *7*, 14752. https://doi.org/10.1038/s41598-017-15309-5

Bertiger, W., Bar-SeverDorsey, Y. A., Haines, B., Harvey, N., Hemberger, D., Hemberger, D., et al. (2020). GipsyX/RTGx, a new tool set for space geodetic operations and research. *Advances in Space Research*, *66*(3), 469–489. https://doi.org/10.1016/j.asr.2020.04.015

Bevis, M., Kendrick, E., Smalley, R., Dalziel, I., Caccmise, D., Sasen, I., et al. (2009). Geodetic measurements of vertical crustal velocity in West Antarctica and the implications for ice mass balance. *Geochemistry, Geophysics, Geosystems*, *10*, Q10005. https://doi.org/10.1029/2009GC002642

Blewitt, G., Kreemer, C., & Hammond, W. C. (2018). Harnessing the GPS data explosion for interdisciplinary science. *Eos*, *99*. https://doi.org/10.1029/2018EO104623

Blewitt, G., Kreemer, C., Hammond, W. C., & Gazeaux, J. (2016). MIDAS trend estimator for accurate GPS station velocities without step detection. *Journal of Geophysical Research: Solid Earth*, *121*, 2054–2068. https://doi.org/10.1002/2015JB012552

Blewitt, G., & Lavallée, D. (2002). Effect of annual signals on geodetic velocity. *Journal of Geophysical Research*, *107*(B7), 2145. https://doi.org/10.1029/2001JB000570

Boehm, J., Werl, B., & Schuh, H. (2006). Troposphere mapping functions for GPS and very long baseline interferometry from European Centre for Medium-Range Weather Forecasts operational analysis data. *Journal of Geophysical Research*, *111*, B02406. https://doi.org/10.1029/2005JB003629

Borsa, A. A., Agnew, D. C., & Cayan, D. R. (2014). Ongoing drought induces uplift in the western United States. *Science*, *345*(6204), 1587–1590. https://doi.org/10.1126/science.1260279

Bos, M., Bastos, L., & Fernandes, R. M. S. (2010). The influence of seasonal signals on the estimation of the tectonic motion in short continuous GPS time-series. *Journal of Geodynamics*, *49*, 205–209. https://doi.org/10.1016/j.jog.2009.10.005

Bürgmann, R., & Chadwell, D. (2014). Seafloor geodesy. *Annual Review of Earth and Planetary Sciences*, *42*, 509–534. https://doi.org/10.1146/annurev-earth-060313-054953

Bürgmann, R., Hilly, G., Ferretti, A., & Novali, F. (2006). Resolving vertical tectonics in the San Francisco Bay Area from permanent scatterer InSAR and GPS analysis. *Geology*, *34*(3), 221–224. https://doi.org/10.1130/G22064.1

Burgette, R. J., Weldon, R. J., & Schmidt, D. A. (2009). Interseismic uplift rates for western Oregon and along-strike variation in locking on the Cascadia subduction zone. *Journal of Geophysical Research*, *114*, B01408. https://doi.org/10.1029/2008JB005679

Carbognin, L., Pietro, T., & Luigi, T. (2005). Land subsidence in the Venetian area: Known and recent aspects. *Giornale di Geologia Applicata*, *1*, 5–11. https://doi.org/10.1474/GGA.2005-01.0-01.0001

Caron, L., Ivins, E. R., Larour, E., Adhikari, S., Nilsson, J., & Blewitt, G. (2018). GIA model statistics for GRACE hydrology, cryosphere, and ocean science. *Geophysical Research Letters*, *45*, 2203–2212. https://doi.org/10.1002/2017GL076644

Cazenave, A., Dominh, K., Ponchaut, F., Soudarin, L., Creteaux, J. F., & Le Provost, C. (1999). Sea level changes from Topex–Poseidon altimetry and tide gauges, and vertical crustal motion from DORIS. *Geophysical Research Letters*, *26*(14), 2077–2080.

Chlieh, M., Perfettini, H., Tavera, H., Avouac, J.-P., Remy, D., Nocquet, J.-M., et al. (2011). Interseismic coupling and seismic potential along the Central Andes subduction zone. *Journal of Geophysical Research*, *116*, B12405. https://doi.org/10.1029/2010JB008166

Church, J. A., Clark, P. U., Cazenave, A., Gregory, J. M., Jevrejeva, S., Levermann, A., et al. (2013). Sea level change. In T. F. Stocker, et al. (Eds.), *Climate change 2013: The physical science basis. Contribution of working group I to the fifth assessment report of the Intergovernmental Panel on Climate Change*. Cambridge, UK/New York. Cambridge University Press.

Church, J. A., & White, N. J. (2011). Sea-level rise from the late 19th century to the early 21st century. *Surveys in Geophysics*, *32*, 585–602. https://doi.org/10.1007/s10712-011-9119-1

Church, J. A., White, N. J., Coleman, R., Lambeck, K., & Mitrovica, J. X. (2004). Estimates of the regional distribution of sea level rise over the 1950–2000 period. *Journal of Climate*, *17*, 2609–2625. https://doi.org/10.1175/1520-0442(2004)017<2609:EOTRDO>2.0.CO;2

Conrad, C. (2013). The solid Earth's influence on sea level. *GSA Bulletin*, *125*(7/8), 1027–1052. https://doi.org/10.1130/B30764.1

Davis, J. L., & Mitrovica, J. X. (1996). Glacial isostatic adjustment and the anomalous tide gauge record of eastern North America. *Nature*, *379*(6563), 331–333.

Davis, J. L., Wernicke, B. P., & Tamisiea, M. E. (2012). On seasonal signals in geodetic time series. *Journal of Geophysical Research*, *117*, B01403. https://doi.org/10.1029/2011JB008690

Dill, R., & Dobslaw, H. (2013). Numerical simulations of global-scale high-resolution hydrological crustal deformations. *Journal of Geophysical Research: Solid Earth*, *118*, 5008–5017. https://doi.org/10.1002/jgrb.50353

Dixon, T. H., Amelung, F., Ferretti, A., Novali, F., Rocca, F., Dokka, R., et al. (2006). Space geodesy: Subsidence and flooding in New Orleans. *Nature*, *441*(7093), 587–588. https://doi.org/10.1038/441587a

Douglas, B. C. (2001). Sea level change in the era of the recording tide gauge. In B. C. Douglas, M. S. Kearney, & S. P. Leatherman (Eds.), *Sea level rise, International Geophysics Series* (Vol. 75, pp. 37–64). London. Academic Press.

England, P., & Molnar, P. (1990). Surface uplift, uplift of rocks, and exhumation of rocks. *Geology*, *18*, 1173–1177.

Faccenna, C., & Becker, T. W. (2010). Shaping mobile belts by small-scale convection. *Nature*, *465*, 602–605.

Famiglietti, J. S., Lo, M., Ho, S. L., Bethune, J., Anderson, K. J., Syed, T. H., et al. (2011). Satellites measure recent rates of groundwater depletion in California's Central Valley. *Geophysical Research Letters*, *38*, L03403. https://doi.org/10.1029/2010GL046442

Faunt, C. C. (2009). Groundwater availability of the Central Valley Aquifer, California. *United States Geological Survey Professional Paper*, *1766*, 225.

Ferreira, L., Marotta, G. S., Madden, E. H., Horbe, A. M. C., Santos, R. V., & Costa, J. M. N. (2020). Vertical displacement caused by hydrological influence in the Amazon Basin. *Journal of Geophysical Research: Solid Earth*, *125*, e2020JB020691. https://doi.org/10.1029/2020JB020691

Fu, Y., Argus, D. F., Freymueller, J. T., & Heflin, M. B. (2013). Horizontal motion in elastic response to seasonal loading of rainwater in the Amazon Basin and monsoon water in Southeast Asia observed by GPS and inferred from GRACE. *Geophysical Research Letters*, *40*, 6048–6053. https://doi.org/10.1002/2013GL058093

Fu, Y., & Freymueller, J. T. (2012). Seasonal and long-term vertical deformation in the Nepal Himalaya constrained by GPS and GRACE measurements. *Journal of Geophysical Research*, *117*, B03407. https://doi.org/10.1029/2011JB008925

Gilfillan, S. M. V., Györe, D., Flude, S., Johnson, G., Bond, C. E., Hicks, N., et al. (2019). Noble gases confirm plume-related mantle degassing beneath Southern Africa. *Nature Communications*, *10*, 5028. https://doi.org/10.1038/s41467-019-12944-6

Hamlington, B. D., Gardner, A. S., Ivins, E., Lenaerts, J. T. M., Reager, J. T., Trossman, D. S., et al. (2020). Understanding of contemporary regional sea-level change and the implications for the future. *Reviews of Geophysics*, *58*, e2019RG000672. https://doi.org/10.1029/2019RG000672

Hamlington, B. D., Thompson, P., Hammond, W. C., Blewitt, G., & Ray, R. (2016). Assessing the impact of vertical land motion on 20th century global mean sea level estimates. *Journal of Geophysical Research: Oceans*, *121*, 4980–4993. https://doi.org/10.1002/2016JC011747

Hammond, W. C., Blewitt, G., & Kreemer, C. (2016). GPS Imaging of vertical land motion in California and Nevada: Implications for Sierra Nevada uplift. *Journal of Geophysical Research: Solid Earth*, *121*, 7681–7703. https://doi.org/10.1002/2016JB013458

Hammond, W. C., Burgette, R., Johnson, K., & Blewitt, G. (2018). Uplift of the Western Transverse Ranges and Ventura area of Southern California: A four-technique geodetic study combining GPS, InSAR, leveling and tide gauges. *Journal of Geophysical Research: Solid Earth*, *122*, 836–858. https://doi.org/10.1002/2017JB014499

Han, S.-C. (2017). Elastic deformation of the Australian continent induced by seasonal water cycles and the 2010–2011 La Niña determined using GPS and GRACE. *Geophysical Research Letters*, *44*, 2763–2772. https://doi.org/10.1002/2017GL072999

Hartnady, C. J. H. (1985). Uplift, faulting, seismicity, thermal spring and possible incipient volcanic activity in the Lesotho-Natal Region, SE Africa: The Quathlamba Hotspot Hypothesis. *Tectonics*, *4*(4), 371–377.

Hawkins, R., Husson, L., Choblet, G., Bodin, T., & Pfeffer, J. (2019). Virtual tide gauges for predicting relative sea level rise. *Journal of Geophysical Research: Solid Earth*, *124*, 391–13391. https://doi.org/10.1029/2019JB017943

Hoggard, M., White, N., & Al-Attar, D. (2016). Global dynamic topography observations reveal limited influence of large-scale mantle flow. *Nature Geoscience*, *9*, 456–463. https://doi.org/10.1038/ngeo2709

Holgate, S. J., Matthews, A., Woodworth, P. L., Rickards, L. J., Tamisiea, M. E., Bradshaw, E., et al. (2013). New data systems and products at the Permanent Service for Mean Sea Level. *Journal of Coastal Research*, *29*(3), 493–504. https://doi.org/10.2112/JCOASTRES-D-12-00175.1

Husson, L., Bodin, T., Spada, G., Choblet, G., & Kreemer, C. (2018). Bayesian surface reconstruction of geodetic uplift rates: Mapping the global fingerprint of glacial isostatic adjustment. *Journal of Geodynamics*, *122*, 25–40. https://doi.org/10.1016/j.jog.2018.10.002

Ivins, E. R., Dokka, R. K., & Blom, R. G. (2007). Post-glacial sediment load and subsidence in coastal Louisiana. *Geophysical Research Letters*, *34*, L16303. https://doi.org/10.1029/2007GL030003

Jiang, Y., Dixon, T. H., & Wdowinski, S. (2010). Accelerating uplift in the North Atlantic region as an indicator of ice loss. *Nature Geoscience*, *3*, 404–407. https://doi.org/10.1038/ngeo845

Johnson, K., Hammond, W. C., Burgette, R., Marshall, S. T., & Sorlien, C. C. (2020). Present-day and long-term uplift across the Western Transverse Ranges of Southern California. *Journal of Geophysical Research: Solid Earth*, *125*, e2020JB019672. https://doi.org/10.1029/2020JB019672

Knowles, L. A., Bennett, R. A., & Harig, C. (2020). Vertical displacements of the Amazon basin from GRACE and GPS. *Journal of Geophysical Research: Solid Earth*, *125*, e2019JB018105. https://doi.org/10.1029/2019JB018105

Kreemer, C., Blewitt, G., & Davis, P. (2020). Geodetic evidence for a buoyant mantle plume beneath the Eifel volcanic area, NW Europe. *Geophysical Journal International*, *222*(2), 1316–1332. https://doi.org/10.1093/gji/ggaa227

Lambeck, K., Smither, C., & Johnston, P. (1998). Sea-level change, glacial rebound and mantle viscosity for northern Europe. *Geophysical Journal International*, *134*, 102–144. https://doi.org/10.1046/j.1365-246x.1998.00541.x

Larsen, C. F., Motyka, R. J., Freymueller, J. T., Echelmeyer, K. A., & Ivins, E. R. (2005). Rapid viscoelastic uplift in southeast Alaska caused by post-Little Ice Age glacial retreat. *Earth and Planetary Science Letters*, *237*, 548–560. https://doi.org/10.1016/j.epsl.2005.06.032

Lithgow-Bertelloni, C., & Silver, P. G. (1998). Dynamic topography, plate driving forces and the African superswell. *Nature*, *395*, 269–272. https://doi.org/10.1038/26212

Loomis, B. D., Luthcke, S. B., & Sabaka, T. J. (2019). Regularization and error characterization of GRACE mascons. *Journal of Geodesy*, *93*, 1381–1398. https://doi.org/10.1007/s00190-019-01252-y

Luthcke, S. B., Sabaka, T. J., Loomis, B. D., Arendt, A. A., McCarthy, J. J., & Camp, J. (2013). Antarctica, Greenland and Gulf of Alaska land ice evolution from an iterated GRACE global mascon solution. *Journal of Glaciology*, *59*(216), 613–631. https://doi.org/10.3189/2013JoG12J147

MacDonald, A. M., Bonsor, H. C., Dochartaigh, B. É. Ó., & Taylor, R. G. (2012). Quantitative maps of groundwater resources in Africa. *Environmental Research Letters*, *7*, 024009. https://doi.org/10.1088/1748-9326/7/2/024009

Marshall, S. T., Funning, G. J., Krueger, H. E., Owen, S. E., & Loveless, J. P. (2017). Mechanical models favor a ramp geometry for the Ventura-Pitas Point fault, California. *Geophysical Research Letters*, *44*, 1311–1319. https://doi.org/10.1002/2016GL072289

Martens, H., Argus, D., Norberg, C., Blewitt, G., Herring, T. A., Moore, A. W., et al. (2020). Atmospheric pressure loading in GPS positions: Dependency on GPS processing methods and effect on assessment of seasonal deformation in the contiguous U.S. and Alaska. *Journal of Geodesy*, *94*, 115. https://doi.org/10.1007/s00190-020-01445-w

Mazzotti, S., Lambert, A., Courtier, N., Nykolaishen, L., & Dragert, H. (2007). Crustal uplift and sea level rise in northern Cascadia from GPS, absolute gravity, and tide gauge data. *Geophysical Research Letters*, *34*, L15306. https://doi.org/10.1029/2007GL030283

Mémin, A., Boy, J.-P., & Santamaría-Gómez, A. (2020). Correcting GPS measurements for non-tidal loading. *GPS Solutions*, *24*, 45. https://doi.org/10.1007/s10291-020-0959-3

Milne, G. A., Gehrels, W. R., Hughes, C. W., & Tamisiea, M. E. (2009). Identifying the causes of sea-level change. *Nature Geoscience*, *2*, 471–478.

Milne, G. A., & Mitrovica, J. X. (1998). Postglacial sea-level change on a rotating Earth. *Geophysical Journal International*, *133*, 1–19.

Mitchum, G. T. (2000). An improved calibration of satellite altimetric heights using tide gauge sea levels with adjustment for land motion. *Marine Geodesy*, *23*, 145–166.

Nerem, R. S., Beckley, B. D., Fasullo, J. T., Hamlington, B. D., Masters, D., & Mitchum, G. T. (2018). Climate-change–driven accelerated sea-level rise detected in the altimeter era. *Proceedings of the National Academy of Sciences of the United States of America*, *115*, 2022–2025. https://doi.org/10.1073/pnas.1717312115

Nerem, R. S., Chambers, D. P., Choe, C., & Mitchum, G. T. (2010). Estimating mean sea level change from the TOPEX and Jason altimeter missions. *Marine Geodesy*, *33*, 435–446.

Nerem, R. S., & Mitchum, G. T. (2002). Estimates of vertical crustal motion derived from differences of Topex/Poseidon and tide gauge sea level measurements. *Geophysical Research Letters*, *29*(19), 1934. https://doi.org/10.1029/2002GL015037

Nyblade, A. A., & Robinson, S. W. (1994). The African superswell. *Geophysical Research Letters*, *21*(9), 765–768. https://doi.org/10.1029/94GL00631

Paysanos, M. E., & Nyblade, A. A. (2007). A top to bottom lithospheric study of Africa and Arabia. *Tectonophysics*, *444*, 27–44.

Peltier, W. R., Argus, D. F., & Drummond, R. (2015). Space geodesy constrains ice age terminal deglaciation: The global ICE-6G_C (VM5a) model. *Journal of Geophysical Research: Solid Earth*, *120*, 450–487. https://doi.org/10.1002/2014JB011176

Pfeffer, J., Spada, G., Mémin, A., Boy, J.-P., & Allemand, P. (2017). Decoding the origins of vertical land motions observed today at coasts. *Geophysical Journal International*, *210*(1), 148–165. https://doi.org/10.1093/gji/ggx142

Pollitz, F. F., Bürgmann, R., & Banerjee, P. (2006). Post-seismic relaxation following the great 2004 Sumatra–Andaman earthquake on a compressible self-gravitating Earth. *Geophysical Journal International*, *167*(1), 397–420. https://doi.org/10.1111/j.1365-246X.2006.03018.x

Prawirodirdjo, L., Ben-Zion, Y., & Bock, Y. (2006). Observation and modeling of thermoelastic strain in Southern California Integrated GPS Network daily position time series. *Journal of Geophysical Research*, *111*, B02408. https://doi.org/10.1029/2005JB003716

Pugh, D., & Woodworth, P. (2014). *Sea-level science*. Cambridge, UK. Cambridge University Press.

Ray, R., Beckley, B. D., & Lemoine, F. G. (2010). Vertical crustal motion derived from satellite altimetry and tide gauges, and comparisons with DORIS measurements. *Advances in Space Research*, *45*(12), 1510–1522. https://doi.org/10.1016/j.asr.2010.02.020

Rebischung, P., Altamimi, Z., Ray, J., & Garayat, B. (2016). The IGS contribution to ITRF2014. *Journal of Geodesy*, *90*, 611–630. https://doi.org/10.1007/s00190-016-0897-6

Riddell, A. R., King, M. A., & Watson, C. S. (2020). Present-day vertical land motion of Australia from GPS observations and geophysical models. *Journal of Geophysical Research: Solid Earth*, *125*, e2019JB018034. https://doi.org/10.1029/2019JB018034

Rodell, M., Famiglietti, J., Wiese, D. N., Reager, J. T., Beaudoing, H. K., Landerer, F. W., & Lo, M.-H. (2018). Emerging trends in global freshwater availability. *Nature*, *557*, 651–659. https://doi.org/10.1038/s41586-018-0123-1

Sandiford, M. (2007). The tilting continent: A new constraint on the dynamic topographic field from Australia. *Earth and Planetary Science Letters*, *261*(1–2), 152–163. https://doi.org/10.1016/j.epsl.2007.06.023

Santamaría-Gómez, A., Gravelle, M., Dangendorf, S., Marcos, M., Spada, G., & Wöppelmann, G. (2017). Uncertainty of the 20th century sea-level rise due to vertical land motion errors. *Earth and Planetary Science Letters*, *473*, 24–32. https://doi.org/10.1016/j.epsl.2017.05.038

Saria, E., Calais, E., Altamimi, Z., Willis, P., & Farah, H. (2013). A new velocity field for Africa from combined GPS and DORIS space geodetic solutions: Contribution to the definition of the African reference frame (AFREF). *Journal of Geophysical Research: Solid Earth*, *118*, 1677–1697. https://doi.org/10.1002/jgrb.50137

Schmid, R., Steigenberger, P., Gendt, G., Ge, M., & Rothacher, M. (2007). Generation of a consistent absolute phase-center correction model for GPS receiver and satellite antennas. *Journal of Geodesy*, *81*, 781–798. https://doi.org/10.1007/s00190-007-0148-y

Schumacher, M., King, M. A., Rougier, J., Sha, Z., Khan, S. A., & Bamber, J. L. (2018). A new global GPS data set for testing and improving modeled GIA uplift rates. *Geophysical Journal International*, *214*, 2164–2176. https://doi.org/10.1093/gji/ggy235

Serpelloni, E., Faccenna, C., Spada, G., Dong, D., & Williams, S. D. P. (2013). Vertical GPS ground motion rates in the Euro-Mediterranean region: New evidence of velocity gradients at different spatial scales along the Nubia-Eurasia plate boundary. *Journal of Geophysical Research: Solid Earth*, *118*, 6003–6024. https://doi.org/10.1002/2013JB010102

Shirzaei, M., & Bürgmann, R. (2018). Global climate change and local land subsidence exacerbate inundation risk to the San Francisco Bay Area. *Science Advances*, *4*(3), eaap9234. https://doi.org/10.1126/sciadv.aap9234

Silverii, F., D'Agostino, N., Métois, M., Fiorillo, F., & Ventafridda, G. (2016). Transient deformation of karst aquifers due to seasonal and multiyear groundwater variations observed by GPS in southern Apennines (Italy). *Journal of Geophysical Research: Solid Earth*, *121*, 8315–8337. https://doi.org/10.1002/2016JB013361

Small, E. E., & Anderson, R. S. (1995). Geomorphically driven Late Cenozoic rock uplift in the Sierra Nevada. *Science*, *270*, 277–281.

Smith-Konter, B. R., Thornton, G. M., & Sandwell, D. T. (2014). Vertical crustal displacement due to interseismic deformation along the San Andreas fault: Constraints from tide gauges. *Geophysical Research Letters*, *41*, 3793–3801. https://doi.org/10.1002/2014GL060091

Sneed, M., Brandt, J., & Solt, M. (2013). Land subsidence along the Delta-Mendota Canal in the northern part of the San Joaquin Valley, California, 2003–10. *United States Geological Survey Scientific Investigations Report 2013-5142*, 87. https://doi.org/10.3133/sir20135142

Stamps, D. S., Saria, E., & Kreemer, C. (2018). A geodetic strain rate model for the East African Rift System. *Scientific Reports*, *8*, 732. https://doi.org/10.1038/s41598-017-19097-w

van Dam, T., Wahr, J., Milly, P. C. D., Shmakin, A. B., Blewitt, G., Lavalleé, D., & Larson, K. M. (2001). Crustal displacements due to continental water loading. *Geophysical Research Letters*, *28*(4), 651–654.

Watkins, M. M., Wiese, D. N., Yuan, D.-N., Boening, C., & Landerer, F. W. (2015). Improved methods for observing Earth's time variable mass distribution with GRACE using spherical cap mascons. *Journal of Geophysical Research: Solid Earth*, *120*, 2648–2671. https://doi.org/10.1002/2014JB011547

Wessel, P., Smith, W. H. F., Scharroo, R., Luis, J., & Wobbe, F. (2013). Generic Mapping Tools: Improved version released. *Eos, Transactions American Geophysical Union*, *94*, 409–410. https://doi.org/10.1002/2013EO450001

White, W. A., & Morton, R. A. (1997). Wetland losses related to fault movement and hydrocarbon production, southeastern Texas coast. *Journal of Coastal Research*, *13*, 1305–1320.

Whitehouse, P. L. (2018). Glacial isostatic adjustment modeling: Historical perspectives, recent advances, and future directions. *Earth Surface Dynamics*, *6*(2), 401–429.

Wise, A., Hughes, C. W., & Polton, J. A. (2018). Bathymetric influence on the coastal sea-level response to ocean gyres at western boundaries. *Journal of Physical Oceanography*, *48*(12), 2949–2964. https://doi.org/10.1175/jpo-d-18-0007.1

Wöppelmann, G., & Marcos, M. (2016). Vertical land motion as a key to understanding sea level change and variability. *Reviews of Geophysics*, *54*, 64–92. https://doi.org/10.1002/2015RG000502

Yamagiwa, S., Miyazaki, S., Hirahara, K., & Fukuhata, Y. (2014). Afterslip and viscoelastic relaxation following the 2011 Tohoku-oki earthquake (M_w 9.0) inferred from inland GPS and seafloor GPS/Acoustic data. *Geophysical Research Letters*, *42*, 66–73. https://doi.org/10.1002/2014GL061735

Zumberge, J. F., Heflin, M. B., Jefferson, D. C., Watkins, M. M., & Webb, F. H. (1997). Precise point positioning for the efficient and robust analysis of GPS data from large networks. *Journal of Geophysical Research*, *102*(B3), 5005–5017. https://doi.org/10.1029/96JB03860